PROTEIN-BASED NANOARCHITECTURES: NANOBIOFABRICATION THROUGH MICROBIAL SURFACE LAYER (S-LAYER) BIOTEMPLATING

A Dissertation

Presented to the Faculty of the Graduate School

of Cornell University

in Partial Fulfillment of the Requirements for the Degree of

Doctor of Philosophy

by

Leonardo Maestri Teixeira

February 2010

PROTEIN-BASED NANOARCHITECTURES: NANOBIOFABRICATION THROUGH MICROBIAL SURFACE LAYER (S-LAYER) BIOTEMPLATING

Leonardo Maestri Teixeira, Ph.D.

Cornell University 2010

The ability to efficiently build and control structures at the nanometer scale using biomolecules is currently an area of very active research. Although natural systems have a vast repertoire of nanostructures able to self-assemble into complex systems, its adoption in industrial nanofabrication process is still a utopian idea. Crystalline bacterial cell surface layer (S-layer) proteins are an example of biological, self-assembled nanostructures that can be exploited for nanotechnology applications. This dissertation focuses on the self-formation of *Lysinibacillus sphaericus* S-layer (SbpA) and the exploitation of its intrinsic properties for nanobiofabrication.

SbpA self-assembly kinetics were studied in detail, as well as, the interaction of SbpA with synthetic surfaces mimicking the natural substrate used as an anchor by SbpA on the bacterial cell surface. It was found that SbpA self-assembles in solution at a rate that is dependent on temperature, the concentration of SbpA, as well as the concentration of calcium ions, and sodium chloride. In addition, SbpA-carbohydrate interaction is dependent on the carbohydrate density, and the net dissociation rate slows with increasing association times. Surface-enhanced Raman spectroscopy (SERS) substrates were bionanofabricated with the aid of a recombinant SbpA, where sub-micromolar concentration levels of 2-mercaptopyridine could be detected, demonstrating the potential of the bionanofabricated SERS substrate using recombinant SbpA.

BIOGRAPHICAL SKETCH

Leonardo Maestri Teixeira received his B.Sc. degree in Dairy Science and Technology from the Universidade Federal de Viçosa (Minas Gerais, BRAZIL) and his M.S in Agricultural Microbiology from the same institution. In his earlier years as an undergraduate student, he worked with Dr. Célia A. de Moraes, where he had the opportunity to enjoy and learn his first steps into the field of microbiology studying the mechanisms of antibiotic resistance in multiresistant microorganisms isolated from poultry carcass. Following the completion of this B.Sc studies, Teixeira enrolled in his M.S. still under the supervision of Dr. Moraes, where he studied the physiology and molecular mechanisms of immunostimulation of a probiotic bacteria.

In August of 2004, Teixeira began his doctoral work in the Department of Microbiology at Cornell University (Ithaca, NY), where he joined Dr. Carl A. Batt's laboratory to study the potential of biomacromolecules for the fabrication of nanostructures.

This work is dedicated to my Grandfather, Moacyr Maestri.

ACKNOWLEDGMENTS

I would like to first acknowledge my mentor Dr. Carl Batt, for the guidance and opportunities he has given me over the last 5 years. I would also like to thank my committee members, Dr. Linda Nicholson and Dr. Peng Chen, whose classes showed me how mesmerizing proteins are.

I am thankful to everybody from the Batt Lab that I had the opportunity to meet, and whose help and friendship was essential for the completion of this dissertation.

I would like to thank my wife, Alessandra, for her friendship and love that makes everything in my life easier and happier. I would also like to thank my parents, Romeu and Esmeralda, and my sister, Renata – Muito obrigado por todo o amor e apoio, sem vocês isto nunca teria sido possível. I would also like to thank my grandfather, Moacyr, for always believing and supporting my dreams. Finally, I would like to thank my daughter, Maria Clara, whose smiles, hugs, and kisses completely changed my perspective of the real valuable things of my life.

TABLE OF CONTENTS

LIST OF FIGURES

CHAPTER 1 - INTRODUCTION: USE OF PROTEINS AS FABRICATION TOOLS IN NANOTECHNOLOGY

Bioinspired Nanotechnology

The ability to build and control structures at the nanometer scale fascinates scientists, as the development of new and more efficient materials and devices would be possible. However, efficient and precise control over materials at the nanometer scale is still challenging. Natural systems possess several examples of nanostructures with intrinsic properties of self-assembly into complex systems with defined structure and surface functionalities. A better understanding of how nature builds nanostructures as the use of more efficient systems and methods for nanofabrication becomes feasible will open new technological frontiers by mimicking or directly using biomaterials in the field of nanotechnology.. Several examples of biomacromolecules, such as DNA, lipids, and proteins have been shown to have great potential for use in nanotechnology (For reviews see (1-5)). Here we will focus on the potential use of proteins as a new tool in the field of nanotechnology, reporting recent successful examples of feasibility studies and their potential use in this field.

The deep know-how that has been accumulated over the last several years about the mechanisms of protein folding, protein engineering, protein-protein and protein-substrate interactions, and well as protein production and purification, has provided a collection of building blocks with great potential to be used as tools in nanotechnology. An important characteristic of proteins that makes them a potential tool in this field is their ability to self-assemble into complex supramolecules. Self-assembly is the spontaneous association by non-covalent interaction of species under equilibrium conditions into a stable and structure defined aggregate. The use of self-assembly in nanotechnology has been broadly studied as an alternative for conventional nanofabrication processes, in the so called bottom-up strategy.

In this review we summarize successful examples of protein-based systems used in nanotechnology. Though reports showing the possible use of several protein

systems in nanotechnology are found in the literature, this review focuses on four specific examples (*i.e.* Ferritin, Tubulin, Amyloid fibers, and S-layers), as numerous groups have reported their versatility and potential exploitation for the field. Examples of protein use include: (i) scaffold for direct biotemplating and use in bottom-up nanofabrication process; (ii) biomaterials in which its nanoscale dimensions are explored to produce materials with functional and/or enhanced properties; and (iii) biosensor systems.

Ferritin

Ferritin is a ubiquitous self-assembling globular protein composed of 4 α-helix bundle that fold and interact through hydrophobic interactions along the α-helix surfaces into a hollow cage-like structure (Figure 1.1A). It is found in many organisms all over the plant, animal and microbial kingdoms where it is used as an iron storage and mineralization system. Two sizes of ferritin are more often found in nature, one with 24 subunits, and one with 12 subunits, named maxi- and mini-ferritin, respectively. The iron is stored within the protein shell as a nanoparticle with a structure similar to the mineral ferrihydrite. A ferritin without the iron nanoparticles within its core is called apoferritin. Apoferritin is a cage shaped supramolecule with the center and inner diameters of 12 nm and 7 nm, respectively. This supramolecule is one of the most studied and characterized biomolecule to be used for the synthesis of nanoparticles, and its use as scaffold for biotemplating of nanoparticles has also been reported (9, 10)

Nanoparticle synthesis of several semiconductor, metal, metal oxide, and magnetic materials was reported with success into the apoferritin core, for example; Semiconductor nanoparticles of CdS, ZnSe, and CdSe were already synthesized using apoferritin. Cadmium sulfide nanoparticles were the first semiconductor nanoparticles

to be synthesized into the apoferritin core in 1996 (11). The strategy used in this first report was the sequential addition of Cd(II) followed by the addition of aqueous sulfide. Even though small CdS nanoparticles of 2.5 nm and 4 nm were synthesized using this strategy, the size could be slightly controlled by the ratio of Cd(II) ions and apoferritin added to the reaction. After the demonstration of the feasibility of synthesizing small CdS semiconductor nanoparticles into the apoferritin core, larger semiconductor nanoparticles of CdSe were synthesized by using a slower reaction method, as Cd^{2+} and Se^{2-} reacts too fast in solution, not allowing the core formation into the apoferritin interior. For CdSe nanoparticle synthesis into the apoferritin core using the slow reaction strategy, Cd^{2+} had to be stabilized by the addition of an excess of ammonia, and Se^{2-} was supplied from selenourea, which slowly degrades in aqueous solution. By using this elegant strategy to slow the reaction rate, the formation of a CdSe core outside the apoferritin became slower than the reaction rate into its cavity, allowing the growth of larger (~ 7 nm) CdSe nanoparticles (12). In a recent article, CdSe nanoparticles were synthesized in apoferritin with the aid of EDTA (13). The strategy used in this new report with the aid of EDTA resembles the previous one for the synthesis of CdSe, as EDTA was used to stabilize Cd^{2+} by forming Cd^{11}-EDTA species and Se^{2-} was supplied as NaHSe. The slow release of Cd^{2+} and Se^{2-} from the precursors allowed its flow into the apoferritin cavity and formation of semiconductor CdSe nanoparticles with a mean diameter of 4.2 nm. Figure 1.1C illustrates the overall strategy used in this report for the slow synthesis of CdSe nanoparticles. The feasibility of synthesizing metal oxide nanoparticles in the apoferritin cavity was demonstrated for different metal complexes. Several approaches were used for the synthesis of the different metallic nanoparticles; however, the general idea shared by all approaches is that the metal ions specifically bind to specific domains of the protein in the apoferritin cavity, which is then reduced by a reductant

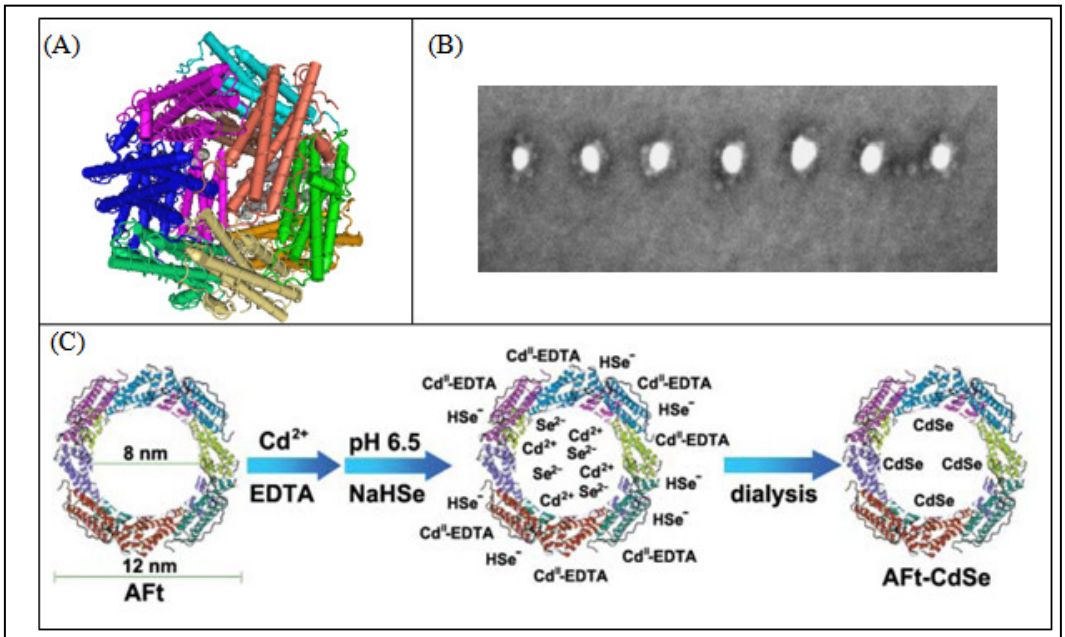

Figure 1.1. (**A**) Graphic representation from *Brucella Melitensis* ferritin structure (**B**) SEM image of a gold binding peptide fused to ferritin and selectively adsorbed onto Au-disks patterned on a SiO_2 (Modified from ref. 18), (**C**) The overall strategy used for the slow fabrication of apoferritin-coated CdSe-QD with the aid of EDTA (Modified from ref. 13).

added to the reaction. When the metal ions are reduced they give rise to the nucleation and growth of the metallic nanoparticles. Even though a general approach is shared for the synthesis of metallic nanoparticles into the apoferritin cavity, the specific procedures and requirements differ for the synthesis of the different metallic nanoparticles. Examples of such diverse requirements include (i) synthesis of nickel sulfate nanoparticles into the apoferritin cavity, which requires carbonated ions in the reaction (14), (ii) synthesis of cobalt nanoparticles, which do not require carbonated ions, but the crystallinity of the synthesized nanoparticles can be controlled by simply adjusting the reaction's temperature (15).

Additionally, different approaches have been optimized to explore the ferritin surface around the synthesized nanoparticles as anchor domains for the specific placement of the nanoparticles at different substrates with nanoscale control. Yamada and collaborators (16) were able for the first time to adsorb single ferritin molecules on a 15 nm pattern of 3-aminopropyltriethoxysilane (APTES) placed at intervals of 100 nm by controlling its electrostatic interactions. In this article, the authors performed a numerical analysis which demonstrated that by manipulating the Debye length they could control the selective adsorption of single ferritin molecules onto the nanopatterned APTES areas, which were then demonstrated experimentally by varying the ionic strength of the buffer used in the adsorption experiment. Another strategy used to achieve the control of the adsorption and positioning of ferritin coated nanoparticles fuses peptides with specific affinities to the ferritin protein surface. By using this approach, Yamashita and collaborators (17) genetically fused a hexapeptide with affinity to titanium at the N-terminus of the L-type subunit of a horse-spleen ferritin subunit, since the N-termini of unmodified recombinant ferritin is known to be located on the outer surface of the protein shell. In this experiment, ferritin with Fe and Co nanoparticles was selectively adsorbed onto Ti nanopatterns, previously formed on a SiO_2 film substrate. In another article from Ishikawa and collaborators (18), a gold binding peptide was genetically incorporated on the N-terminus of the recombinant L-chain apoferritin. The specific adsorption of the recombinant ferritin with iron nanoparticles to a gold surface was examined using a quartz crystal microbalance, and also assessed by comparing the protein's adsorption to gold nanopatterns previously fabricated on a SiO_2 surface. Through the use of the gold binding peptide fused to the recombinant ferritin, the coated iron nanoparticles had its specific adsorption increased by three-fold, when 1% of Tween 20 – known to reduce nonspecific interactions - was incorporated in the experiment buffer (Figure 1.1C).

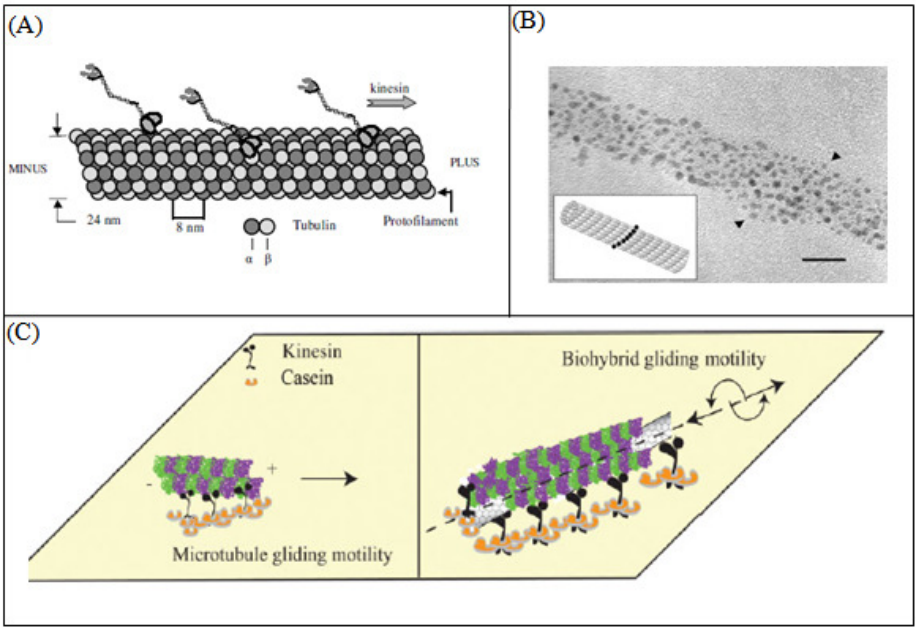

Figure 1.2. (**A**)Microtubule (MT) structure showing the 24 hollow tubes formed by the self-assembly of tubulins. Kinesin moves the microtubule with 8 nm steps along the MT surface towards the plus end (Modified from ref. 39), (**B**). Palladium nanoparticle array densely immobilized on a microtubule surface, with arrows and inset showing the microtubule helical template (Modified from ref. 27), (**C**) Functional properties of the tubulin-MWNT hybrids, where in the left is a representation of the microtubule gliding and biohybrids movement on kinesin coated surfaces, and in the right the linear motility of biohybrid gliding on a kinesin coated surface (Modified from ref. 53)

Tubulin

Tubulin is a globular protein widely found in eukaryotes that performs essential roles in the cell's life, e.g. maintenance of cell shape, cell motility, separation of chromosomes during mitosis, and organelle transport. Tubulin is the building block

of microtubules (MTs), and each tubulin subunit is an asymmetric heterodimer comprised of an α and a β tubulin. Tubulin possesses the ability to self-assemble in a non-equilibrium way both *in vivo* and *in vitro* in a process known as dynamic instability (19, 20). The asymmetry of the subunits and the head-to-tail assembly in parallel protofilaments give MTs an overall structural polarity (Figure 1.2A). The self-assembly of tubulin *in vitro* for the formation of MTs occurs at physiological conditions (i.e. pH, temperature, and ionic strength), and requires GTP as *in vivo* (21). The formed MTs are highly ordered α,β-tubulin heterodimers helically arranged, and its structure is partially stabilized by a layer of GTP tubulin at its end (22, 23). Depending on the self-assembly reaction conditions, tubulin can self-assemble in a variety of polymorphs, e.g. sheets, ribbons, rings, and spirals (24-26).

Different tubulin biopolymers have been used as scaffold for the synthesis of different metal nanoparticles *in situ*, where the formed inorganic nanoparticles are organized in a structure that resembles the biopolymer original morphology. Different metallic nanoparticles were synthesized with success at the conserved surface's biopolymer (27-29), and the concept of how the nanoparticles synthesis occurs is similar to the general approach used for the synthesis of nanoparticles in other biomolecules, such as ferritin that are used as scaffold for metal nanoparticles formation. Metal nanoparticle synthesis on biopolymers of tubulin may be controlled by the different reaction synthesis conditions, such as pH, temperature, metal ion concentration, and the different types of metal ions and reductant used. For example, it was found that Na_2PdCl_4 when reduced with trisodium citrate at 90 ^oC produces small Pd clusters of approximately 1.9 nm; however, when dimethylamine borane was used as a reducing agent instead, larger Pd nanoparticles of 3.1 nm were formed (27). Figure 1.2B shows a densely immobilized Pd nanoparticles on MTs surface. The different morphologies that tubulin is able to form when self-assembled *in vitro* has

also been explored as an alternative in bottom-up nanofabrication strategies. In one example, metal ring nanostructures were synthesized by the deposition of metals on the ring shaped tubulin assemblies. The assembly of tubulins in a ring or spiral structure, instead of MTs, can be accomplished by adding Ca^{2+} to the assembly reaction, demonstrating the simplicity and versatility of the system (30). MTs have also been used in conjunction with kinesin as biomolecular motors for the transport of nanocomposites. Kinesin are motor proteins that transport cargos unidirectionaly along the MTs in a cell. It is a heterotetramer protein composed of two identical kinesin heavy chains, and two kinesin light chains. The heavy chains or motor chains move along the MT in 8 nm steps by converting the energy of ATP hydrolysis into movement. The light chains are terminated by a binding region that is normally used *in vivo* to transport intracellular cargo. The asymmetry of the tubulin subunits and the head-to-toe arrangement gives the MTs a structural lattice that is recognized by kinesin. Kinesin moves only from the minus to the plus end of MTs, where the minus end is terminated with α tubulin, and the plus end, which is kinetically more dynamic, terminated with β-tubulin.

Different versions of the kinesin-MT system were investigated as a way for transporting nano scale cargos, and the two main design strategies for this purpose have particular advantages and disadvantages. In one design the MTs are fixed to the surface, and the kinesin moves along them like in a railroad (31). In the other design the approach is inverted, where kinesins are the proteins immobilized on the surface and the microtubules are then propelled throughout the surface by the immobilized kinesins (Figure 1.2C) (32). The advantage of the first design is the ability of transporting larger objects coated with kinesin, and the advantage of the latter, also known as the inverted motility strategy, is that it possesses more capabilities for engineering of the tracks with more precise configurations, as the physical limitations

of immobilizing larger microtubules onto surfaces are absent. Examples of cargos that were successfully transported by these systems include CdSe quantum dots (32), fluorescent molecules (33), microspheres (34), silicon microchips (35), and DNA molecules (36).

This chemomechanical mechanism creates many applied opportunities as it can be used to shuttle cargos, power fluids in micro and nanofluidics, sort and selectively deliver nanocargos, and in nanoelectromechanical systems (NEMS). One example of such practical use of the kinesin-MTs system is the one demonstrated by Lin and collaborators (33), in which a microfluidic chip was built, and a detection sensitivity two orders of magnitude higher than typical immunoassays, such as ELISA, was achieved by exploring the biomolecular motor of the Kinesin-MTs for sorting, transport, and concentration of the analytes.

Amyloid Fibers

Amyloid fibers are self-assembled products formed from proteins or peptides that suffer a structural transition from the native and soluble conformation into the aggregated fibrillar assemblies. They are remarkably stable and its structure is rich in β-sheets which stabilize the final aggregates by the hydrogen bonds between them. It possesses a diameter that ranges from 7 to 10 nm, and can reach up to micron sizes in length. Figure 1.3A illustrates the overall process employed for the formation of amyloid fibrils. Several diseases are caused by the formation of amyloid fibrils, such as type II diabetes (37, 38), Parkinson's disease (39), prion disorders, and Alzheimer's disease (40, 41). The ability to assemble at physiological conditions *in vitro*, in addition to its higher than the average protein mechanical strength, chemical, and physical stability, makes amyloid fibers potential building blocks for the construction of new biomaterials. The assembly conditions of amyloid fibers can be controlled to

form fibrils with different lengths and properties; for example, at high concentration of protein monomers and under high turbulence, short fibers with a homogeneous length distribution are produced. However, when a ratio of 1:64 of short fibers to protein monomers are used in the self-assembly reaction, fibers with several hundred micrometers are produced (Figure 1.3B) (42).

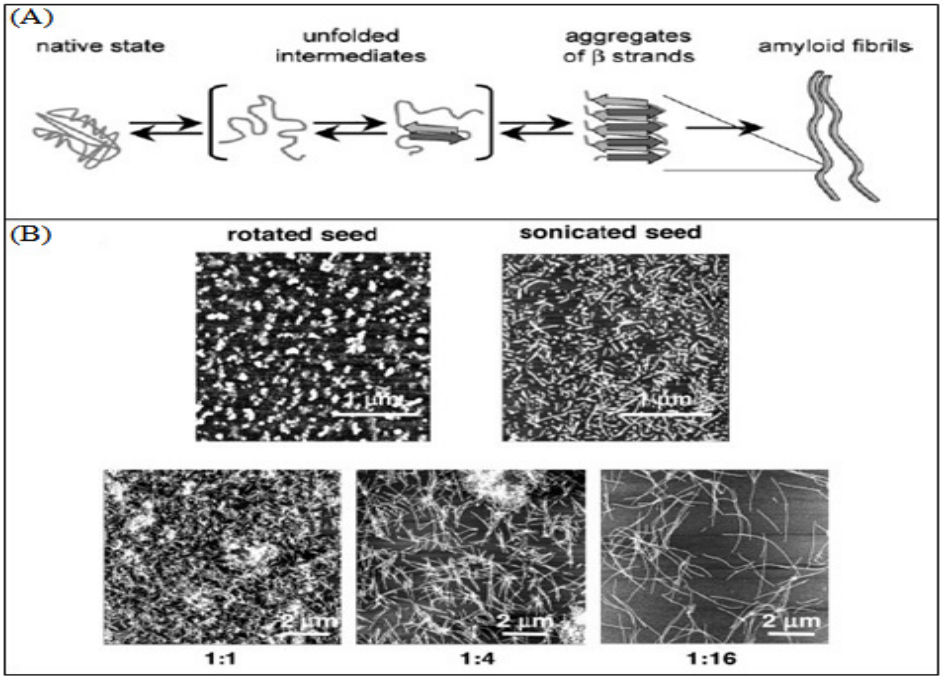

Figure 1.3. (**A**) Schematic representation of the formation of amyloid fibrils, where a folded monomers experience a conformational transition to a beta-sheet state that self-assemble into ladders of beta-strands that then aggregates into amyloid fibrils (Modified from ref. 54), (**B**) Formed amyloid fibers with the N-terminus and middle region (NM) of Sup35p, where increasing the soluble NM concentration over the seed concentration led to increased fiber lengths. At ratios of 1:16 of seed: soluble fibers with over 6 µm were formed (modified from ref. 42)

Several research groups have exploited fibrils for the synthesis of new nanomaterials with different properties such as nanowires (42), and as bio-scaffolds for inorganic materials (e.g. nanoparticles (42)) and organic materials (e.g. biotin (43) and cytochromes (44)). The fabrication of nanowires using amyloid fibrils was first accomplished using a genetically modified amyloidogenic N-terminus and the middle region (NM) of Sup35p from *Saccharomyces cerevisiae*. The protein was modified to add a cysteine residue that remained accessible at the surface of the fibrils after formation. Nanogold monomaleimide® was then covalently linked to the fibers through the maleimide-thiol reaction, and this incorporation of nanoparticles to the fibrils affected neither its final stability nor morphology. Nanowires were then formed by the directional deposition and reduction of silver and gold ions using the gold nanoparticles as seeds. The NM fibrils, which were initially insulators without the metal coating became very good conductive materials after the metal deposition/reduction (42). In another article, an attempt to mimic natural conductive nanowires, amyloid fibrils were functionalized with cytochrome b allowing the incorporation of heme molecules on the amyloid fibril surface (44). The information obtained by studying how amyloid fibers are formed allowed several groups to design and synthesize artificial amyloid fibers, which have been shown to be of great promise for the rational design of new bioinspired nanomaterials (1, 45).S-layer proteins

S-layer proteins are found as a 2-D crystalline array on the outermost envelope of many bacterial species and in the majority of *Archaea* (46). They are composed of identical protein or glycoprotein monomers with molecular weight ranging from 40 to 200 kDa depending on the microorganism in which it is found. The crystalline array formed displays a highly repetitive structure with the center-to-center lattice ranging from 5 to 30 nm, and with two or more distinct classes of pores with identical morphology and size in the range of 2 to 8 nm. The surface topography and

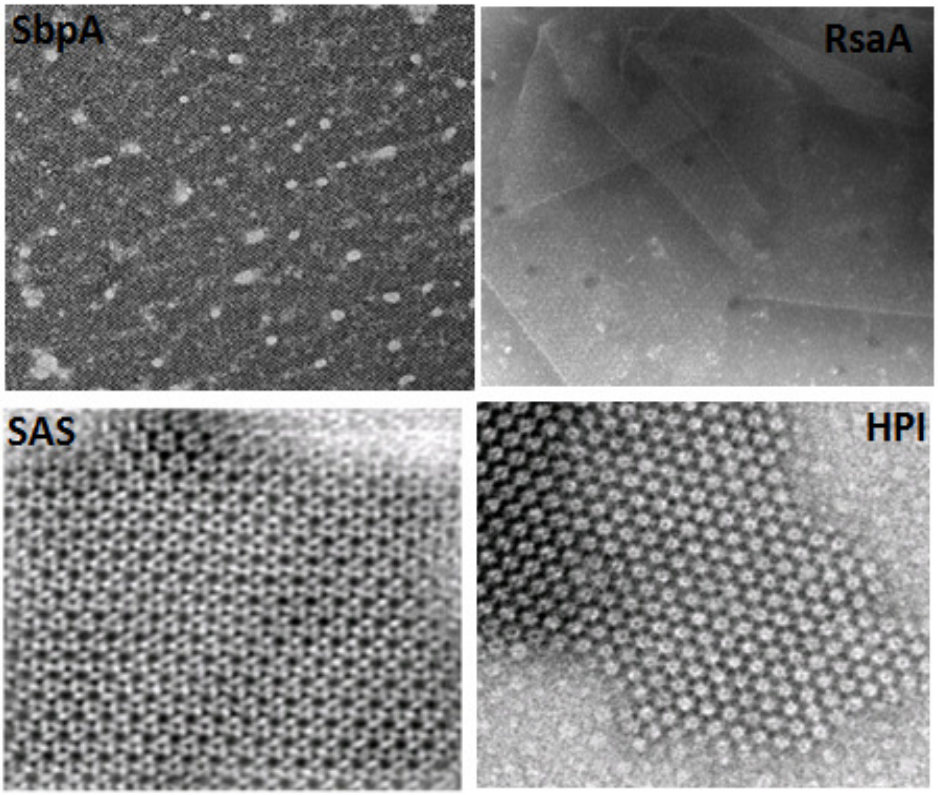

Figure 1.4. TEM (negative stained) of different S-layers, where SbpA is the S-layer from *Lysinobacillus sphaericus* that possess a p4 symmetry, RsaA is the S-layer from *Caulobacter crescentus* that possess p6 symmetry, SAS is the S-layer from *Sulfolobus acidocaldarius* that possess p6 symmetry, and HPI is the S-layer from *Deinococcus radiodurans* that possess p6 symmetry. SbpA and RsaA have the ability to self-assemble *in vitro* with already optimized procedures; however a protocol for *in vitro* self-assembly of SAS and HPI has not been made available to date.

physicochemical properties of the extracellular and intracellular sides of the protein array are notably different, where a 'smoother' surface is generally exposed to the external aqueous environment, and a more 'corrugated' surface is usually attached to the underlying cell wall [8, 9]. Figure 1.4 shows examples of S-layers from different

microorganisms. One particular characteristic of certain types of S-layer proteins is their ability to self-assemble *in vitro* into the same array as found *in vivo* into monolayer sheets that may feature an oblique (p1, p2), square (p4) or hexagonal (p3, p6) lattice symmetry. *In vivo*, the synthesis, secretion, and self-assembly of the S-layer monomeric units are performed in a rate synchronized with the microorganism cell growth and division. The recrystallization of S-layers from different microorganisms has already been demonstrated *in vitro* in suspension, at liquid-surface interfaces, on lipid structures, and on solid supports. [6, 10-15]. The feasibility of exploiting the nanoscale features of S-layers for nanotechnological applications has been demonstrated by several groups. Such S-layer use lends itself to various applications, especially its utilization as a scaffold for the organization of inorganic materials with nanoscale precision as an alternative in nanofabrication process (6, 47). Further, it can be used for the *in situ* synthesis of nanoparticles (48) and as crystalline protein mask in nanofabrication (49). S-layer may also function as a scaffold for functional biomolecules (50). The feasibility of using S-layers as scaffolds for the positioning of pre-formed nanoparticles to form arrays has been demonstrated using different S-layer proteins (*i.e. Deinococcus radiodurans* (7, 51), *Sulfolobus acidocaldarius* (51), and *L. sphaericus* (52)). Arrays of preformed nanoparticles of different materials, such as metals (6, 7, 52), and semiconductors (7) have also been biotemplated with the aid of S-layers. Mark, S.S. and collaborators (7) improved the patterning of inorganic nanoparticles (*i.e.* metallic and semiconductor) on both *S. acidocaldarius* and *D. radiodurans* S-layers by manipulating the physicochemical conditions of the adsorption reaction, as well as the chemical composition of the nanoparticles used. Arrays of different geometrical arrangements were produced through the use of the two S-layers tested. This study also demonstrated that the geometry of the formed nanoparticle arrays may be modified by using different types of functional groups

reacting to the nanoparticle surface (*i.e*. negative- or positive-charged, and short- or long-chain length). In another work, Mark, S.S. and collaborators (51) demonstrated that by encapsulating platinum nanoparticles with dendrimers allowed the formation of highly periodic arrays of pre-synthesized nanoparticles using S-layer proteins as biotemplate. Recent studies have fused affinity tags in conjunction, or not, with reactive amino acids (52) in search of a way to improve the specific binding of functional organic or inorganic materials to the S-layer array, since stronger or covalent interactions can be employed, *e.g*. biotin-streptavidin, thiol-maleimide. The ability to genetically modify S-layers is of great promise, as it allows the enhancement of its functional and potential applied functions without compromising their intrinsic properties, such as the ability to self-assemble into arrays with controlled and precise nanoscale topography. The applicability of the nanoparticle arrays formed with the aid of the S-layer scaffolds were further demonstrated when nanopillars were fabricated using the nanoparticles in the array the seed for its growth (6). However, this first attempt to demonstrate the ability to further build structures in a bottom-up strategy using the biotemplated nanoparticles lacked the ability to maintain and translate the ordering of the seed array of nanoparticles to the nanopillar array formed. Yet, in another article, the production of vertically oriented nanowires with high density was successfully accomplished by a bottom-up strategy. The strategy employed an array of biotemplated gold nanoparticles for the growth of Germanium nanowires (47). In this work, the biotemplated ordered array of the gold nanoparticles were better translated into the formed Germanium nanowires, and the production of vertically oriented nanowires with high density was successfully accomplished by this bottom-up strategy.

Conclusion

Though several reports demonstrated the feasibility of using proteins as "biotools" for nanotechnological applications, it has become clear that it is indeed feasible to use proteins as biotools for nanotechnological applications, but industry still lags in adoption of these potential strategies. However, with the significant developments that have been made in the specific area of biomaterials over the last years, as well as the protein versatility shown by the above examples, proteins will soon assume an important role in the field of nanobiotechnology, as new processes and bioinspired materials emerge. The translation of the recent findings from the field of protein science, in addition to the information accumulated by the pharma industry for its large scale production and purification, may accelerate the adoption of proteins for nanotechnological applications.

REFERENCES

1. Banta, S., Z. Megeed, M. Casali, K. Rege, and M. L. Yarmush. 2007. Engineering protein and peptide building blocks for nanotechnology. J. Nanosci. Nanotechnol., 7:387-401.

2. Condon, A. 2006. Designed DNA molecules: principles and applications of molecular nanotechnology. Nat. Rev. Genet., 7:565-575.

3. Perrie, Y. 2009. Liposomes, lipid assemblies, nanotechnology, and everything interesting in between. J. Liposome Res., 19:1.

4. Seeman, N. C. 2007. An overview of structural DNA nanotechnology. Mol. Biotechnol., 37:246-257.

5. Vo-Dinh, T. 2005. Protein nanotechnology: the new frontier in biosciences. Methods Mol. Biol., 300:1-13.

6. Mark, S. S., M. Bergkvist, P. Bhatnagar, C. Welch, A. L. Goodyear, X. Yang, E. R. Angert, and C. A. Batt. 2007. Thin film processing using S-layer proteins: biotemplated assembly of colloidal gold etch masks for fabrication of silicon nanopillar arrays., Colloids Surf. B Biointerfaces 57:161-173.

7. Mark, S. S., M. Bergkvist, X. Yang, L. M. Teixeira, P. Bhatnagar, E. R. Angert, and C. A. Batt. 2006. Bionanofabrication of metallic and semiconductor nanoparticle arrays using S-layer protein lattices with different lateral spacings and geometries., Langmuir 22:3763-3774.

8. Lee, S. H., and C. Mao. 2004. DNA nanotechnology. Biotechniques, 37:517-519.

9. Matsui, T., N. Matsukawa, K. Iwahori, K. Sano, K. Shiba, and I. Yamashita. 2007. Realizing a two-dimensional ordered array of ferritin molecules directly on a solid surface utilizing carbonaceous material affinity peptides., Langmuir 23:1615-1618.

10. Yuan, Z., D. N. Petsev, B. G. Prevo, O. D. Velev, and P. Atanassov. 2007. Two-dimensional nanoparticle arrays derived from ferritin monolayers. Langmuir, 23:5498-5504.

11. Kim, K. W. W., and M. Stephen. 1996. Biomimetic synthesis of cadmium sulfide-ferritin nanocomposites. Advanced Materials, 8:928-932.

12. Yamashita, I., J. Hayashi, and M. Hara. 2004. Bio-template Synthesis of Uniform CdSe Nanoparticles Using Cage-shaped Protein, Apoferritin. Chemistry Letters, 33:1158-1159.

13. Xing, R., X. Wang, L. Yan, C. Zhang, Z. Yang, and Z. Guo. 2009. Fabrication of water soluble and biocompatible CdSe nanoparticles in apoferritin with the aid of EDTA. Dalton Trans., 1710-1713.

14. Okuda, M., K. Iwahori, I. Yamashita, and H. Yoshimura. 2003. Fabrication of nickel and chromium nanoparticles using the protein cage of apoferritin. Biotechnol. Bioeng., 84:187-194.

15. Allen, M., D. Willits, M. Young, and T. Douglas. 2003. Constrained synthesis of cobalt oxide nanomaterials in the 12-subunit protein cage from Listeria innocua. Inorg. Chem., 42:6300-6305.

16. Yamada, K., S. Yoshii, S. Kumagai, I. Fujiwara, K. Nishio, M. Okuda, N. Matsukawa, and I. Yamashita. 2006. high-density and highly surface selective adsorption of protein-nanoparticle complexes by controlling electrostatic interaction Japanese Journal of Applied Physics, 45:4259-4264.

17. Yamashita, I., H. Kirimura, M. Okuda, K. Nishio, K. Sano, K. Shiba, T. Hayashi, M. Hara, and Y. Mishima. 2006. Selective nanoscale positioning of ferritin and nanoparticles by means of target-specific peptides. Small, 2:1148-1152.

18. Ishikawa, K., K. Yamada, S. Kumagai, K.-I. Sano, K. Shiba, I. Yamashita, and M. Kobayashi. 2008. Adsorption Properties of a Gold-Binding Peptide Assessed by its Attachment to a Recombinant Apoferritin Molecule. Applied Physics Express, 1:034006.

19. Idriss, H., D. K. Stammers, C. K. Ross, and R. G. Burns. 1991. The dynamic instability of microtubules is not modulated by alpha-tubulin tyrosinylation. Cell Motil. Cytoskeleton, 20:30-37.

20. Mitchison, T. J., and M. W. Kirschner. 1987. Some thoughts on the partitioning of tubulin between monomer and polymer under conditions of dynamic instability. Cell Biophys., 11:35-55.

21. Lin, C. M., and E. Hamel. 1987. Interrelationships of tubulin-GDP and tubulin-GTP in microtubule assembly. Biochemistry, 26:7173-7182.

22. Chretien, D., I. Jainosi, J. C. Taveau, and H. Flyvbjerg. 1999. Microtubule's conformational cap. Cell Struct. Funct., 24:299-303.

23. Janosi, I. M., D. Chretien, and H. Flyvbjerg. 2002. Structural microtubule cap: stability, catastrophe, rescue, and third state. Biophys. J., 83:1317-1330.

24. Langford, G. M. 1978. In vitro assembly of dogfish brain tubulin and the induction of coiled ribbon polymers by calcium. Exp. Cell Res., 111:139-151.

25. Matsumura, F., and M. Hayashi. 1976. Polymorphism of tubulin assembly. In vitro formation of sheet, twisted ribbon and microtubule. Biochim. Biophys. Acta, 453:162-175.

26. Zeeberg, B., J. Cheek, and M. Caplow. 1980. Exchange of tubulin dimer into rings in microtubule assembly-disassembly. Biochemistry, 19:5078-5086.

27. Behrens, S., K. Rahn, W. Habicht, K. J. Böhm, H. Rösner, E. Dinjus, and E. Unger. 2002. Nanoscale Particle Arrays Induced by Highly Ordered Protein Assemblies. Advanced Materials, 14:1621-1625.

28. Silke, B., H. Wilhelm, W. Jin, and U. Eberhard. 2006. Tubulin assemblies as biomolecular templates for nanostructure synthesis: from nanoparticle arrays to nanowires. Surface and Interface Analysis, 38:1014-1018.

29. Behrens, S., J. Wu, W. Habicht, and E. Unger. 2004. Silver Nanoparticle and Nanowire Formation by Microtubule Templates. Chemistry of Materials 16:3085-3090.

30. Behrens, S., W. Habicht, K. Wagner, and E. Unger. 2006. Assembly of Nanoparticle Ring Structures Based on Protein Templates. Advanced Materials, 18:284-289.

31. Limberis, L., J. J. Magda, and R. J. Stewart. 2001. Polarized Alignment and Surface Immobilization of Microtubules for Kinesin-Powered Nanodevices. Nano Letters, 1:277-280.

32. Bachand, G. D., S. B. Rivera, A. K. Boal, J. Gaudioso, J. Liu, and B. C. Bunker. 2004. Assembly and Transport of Nanocrystal CdSe Quantum Dot

Nanocomposites Using Microtubules and Kinesin Motor Proteins. Nano Letters, 4:817-821.

33. Lin, C.-T., M.-T. Kao, K. Kurabayashi, and E. Meyhofer. 2008. Self-Contained, Biomolecular Motor-Driven Protein Sorting and Concentrating in an Ultrasensitive Microfluidic Chip. Nano Letters, 8:1041-1046.

34. Hess, H., J. Clemmens, D. Qin, J. Howard, and V. Vogel. 2001. Light-Controlled Molecular Shuttles Made from Motor Proteins Carrying Cargo on Engineered Surfaces. Nano Letters, 1:235-239.

35. Loren, L., and J. S. Russell. 2000. Toward kinesin-powered microdevices. Nanotechnology, 11:47-51.

36. Diez, S., C. Reuther, C. Dinu, R. Seidel, M. Mertig, W. Pompe, and J. Howard. 2003. Stretching and Transporting DNA Molecules Using Motor Proteins. Nano Letters, 3:1251-1254.

37. Soong, R., J. R. Brender, P. M. Macdonald, and A. Ramamoorthy. 2009. Association of highly compact type II diabetes related islet amyloid polypeptide intermediate species at physiological temperature revealed by diffusion NMR spectroscopy. J. Am. Chem. Soc., 131:7079-7085.

38. Tasaka, Y., F. Nakaya, S. Karibe, and Y. Iwamoto. 1999. Pancreatic amyloid proteins and their relation to clinical diabetes, with special reference to serum insulin secretion. Diabetes Care, 22:1590.

39. Kalaitzakis, M. E., M. B. Graeber, S. M. Gentleman, and R. K. Pearce. 2008. Striatal beta-amyloid deposition in Parkinson disease with dementia. J Neuropathol. Exp. Neurol., 67:155-161.

40. Price, D. L., D. R. Borchelt, and S. S. Sisodia. 1993. Alzheimer disease and the prion disorders amyloid beta-protein and prion protein amyloidoses. Proc. Natl. Acad. Sci. U. S. A., 90:6381-6384.

41. Thompson, A. J., and C. J. Barrow. 2002. Protein conformational misfolding and amyloid formation: characteristics of a new class of disorders that include Alzheimer's and Prion diseases. Curr. Med. Chem., 9:1751-1762.

42. Scheibel, T., R. Parthasarathy, G. Sawicki, X. M. Lin, H. Jaeger, and S. L. Lindquist. 2003. Conducting nanowires built by controlled self-assembly of

amyloid fibers and selective metal deposition. Proc. Natl. Acad. Sci. U. S. A., 100:4527-4532.

43. Taguchi, Y., Z. D. Shi, B. Ruddy, D. W. Dorward, L. Greene, and G. S. Baron. 2009. Specific biarsenical labeling of cell surface proteins allows fluorescent- and biotin-tagging of amyloid precursor protein and prion proteins. Mol. Biol. Cell, 20:233-244.

44. Baldwin, A. J., R. Bader, J. Christodoulou, C. E. MacPhee, C. M. Dobson, and P. D. Barker. 2006. Cytochrome display on amyloid fibrils. J. Am. Chem. Soc., 128:2162-2163.

45. Papapostolou, D., A. M. Smith, E. D. Atkins, S. J. Oliver, M. G. Ryadnov, L. C. Serpell, and D. N. Woolfson. 2007. Engineering nanoscale order into a designed protein fiber. Proc. Natl. Acad. Sci. U. S. A., 104:10853-10858.

46. Sara, M., and U. B. Sleytr. 2000. S-Layer proteins. J. Bacteriol., 182:859-868.

47. Sierra-Sastre, Y., S. Choi, S. T. Picraux, and C. A. Batt. 2008. Vertical growth of Ge nanowires from biotemplated Au nanoparticle catalysts. J. Am. Chem. Soc., 130:10488-10489.

48. Mertig, M., R. Wahl, M. Lehmann, P. Simon, and W. Pompe. 2001. Formation and manipulation of regular metallic nanoparticle arrays on bacterial surface layers: an advanced TEM study. The European Physical Journal D - Atomic, Molecular, Optical and Plasma Physics, 16:317-320.

49. Allred, D. B., M. Sarikaya, F. Baneyx, and D. T. Schwartz. 2005. Electrochemical Nanofabrication Using Crystalline Protein Masks. Nano Letters, 5:609-613.

50. Pleschberger, M., A. Neubauer, E. M. Egelseer, S. Weigert, B. Lindner, U. B. Sleytr, S. Muyldermans, and M. Sara. 2003. Generation of a functional monomolecular protein lattice consisting of an s-layer fusion protein comprising the variable domain of a camel heavy chain antibody. Bioconjug. Chem., 14:440-448.

51. Mark, S. S., M. Bergkvist, X. Yang, E. R. Angert, and C. A. Batt. 2006. Self-assembly of dendrimer-encapsulated nanoparticle arrays using 2-D microbial S-layer protein biotemplates. Biomacromolecules, 7:1884-1897.

52. Badelt-Lichtblau, H., B. Kainz, C. Vollenkle, E. M. Egelseer, U. B. Sleytr, D. Pum, and N. Ilk. 2009. Genetic Engineering of the S-Layer Protein SbpA of Lysinibacillus sphaericus CCM 2177 for the Generation of Functionalized Nanoarrays. Bioconjug. Chem., 20,5:895-903

53 Cerasela Zoica Dinu, Shyam Sundhar Bale, Guangyu Zhu, and Jonathan S. Dordick. 2009. Tubulin Encapsulation of Carbon Nanotubes into Functional Hybrid Assemblies. Small, 5, 3:310-315

54 Izhack Cherny and Ehud Gazit. Amyloids: Not Only Pathological Agents but Also Ordered Nanomaterials. Angewandte Chemie International Edition., 47, 22:4062-4069.

CHAPTER 2 - STUDY OF THE ENTROPICALLY DRIVEN SELF-ASSEMBLY OF *Lysinibacillus sphaericus* S-LAYER PROTEINS*

*Originally published as: Teixeira, LM; Strickland, A.; Mark, SS; Bergkvist M; Sierra-Sastre, Y.; Batt, C. **Entropically driven Self-assembly of *Bacillus sphaericus* S-layer proteins analyzed under various environmental conditions.** Macromolecular Bioscience. (2009). **DOI: 10.1002/mabi.200900175.**

INTRODUCTION

A considerable amount of effort is being put forth to understand the molecular basis of molecular self-assembly, as this can be used in the development of novel types of supramolecular structures and engineered nanomaterials. In nature, a variety of biomolecules have the ability to self-assemble and form organized and defined structures at the molecular level and ranging from microscopic to macroscopic scales (1-5). S-layer proteins are one example of such a class of biomolecules which form a 2-D crystalline array on the outermost envelope component of many bacterial species and in the majority of archaea (6). These crystalline arrays are composed of identical protein (or glycoprotein) monomers with molecular weights that can range from 40-200 kDa depending on the microorganism species. S-layers display a highly repetitive surface structure with center-to-center lattice spacings of 5-30 nm. Furthermore, S-layers typically have two or more distinct classes of pores with identical morphology and size in the range of 2-8 nm. A possible physiological role for S-layer proteins has been suggested based upon *in vitro* experiments which have revealed that these protein layers have ion specificity (7). Significantly, the surface topography and physicochemical properties are different between the extracellular and intracellular sides of S-layer proteins. Whereas a 'smoother' surface is generally exposed to the external aqueous environment, and a more 'corrugated' surface is usually attached to the underlying cell wall (8, 9). One particular characteristic of certain types of S-layer proteins is their ability to self-assemble either *in vivo* or *in vitro* into monolayer sheets featuring an oblique (p1, p2), square (p4) or hexagonal (p3, p6) lattice symmetry. Indeed, isolated subunits of S-layers from a number of bacteria have the capability to recrystallize in suspension, at liquid- surface interfaces, on lipid structures, and on solid supports (6, 10-15).

As demonstrated through a number of recent reports, S-layers from *Bacillaceae* species have great promise for use in nanotechnological applications (11, 16-20). *Bacillaceae* S-layers have an N-terminal region named the S-layer homology (SLH) domain that is responsible for anchoring the protein subunits to secondary cell wall polymers (SCWPs) in the underlying rigid cell envelope layer (21). SLH domains are one of only a few common structural components that are known to exist in S-layer proteins of selected microorganism species (11, 22-25). S-layers from *Lysinibacillus sphaericus* (SbpA) – previous known as *Bacillus sphaericus* - show a square symmetry, with a center-to-center spacing of the morphological units of 13.1 nm, composed of protein monomers with 129 kDa. Several works have shown that truncated and fused recombinant SbpA protein retain their ability to self-assemble *in vitro,* thus confirming their potential technological usefulness (11, 18, 19, and 26).

While notable progress has been made in assessing the technological potential of S-layers (27-30), there is currently no high-resolution structural data of a full protein available for members of this class of proteins (31-33). Because of this lack of structural information, recently cysteine residues were incorporated by point mutations on the S-layer protein from *Geobacillus stearothermophilus* PV72/p2 to be used to map the location of those individual residues in the protein surface (34). Furthermore, although self-assembly is one of the most distinctive characteristics of S-layers, only a limited number of studies have been carried out to understand this mechanism. To our knowledge, the only relative in-depth investigation of the *in vitro* self-assembly process of S-layers was reported more than 20 years ago by Jaenicke and collaborators using the S-layer protein from *Bacillus stearothermophilus* (35).

The objective of this paper is to understand how SbpA monomers alone drive the self-assembly reaction, and how the different environmental conditions influence this reaction, which was accomplished by isolating the protein-protein interaction

performing the experiments in solution. In particular, such fundamental knowledge will ultimately enable the rational design of long-range ordered single-crystal protein arrays, which will be essential for fully exploiting the functional utility of S-layer components in nanobiotechnology-based applications such as miniaturized nanoelectronics (36), and ultra-fast quantum computing (37). With the objective described above in mind, we followed the *in vitro* self-assembly kinetics of SbpA in real time under different solution conditions by dynamic light scattering (DLS) and absorption spectrophotometry techniques. The results obtained here indicated that the SbpA self-assembly process driven by the protein monomers is sensitive to different physical and chemical conditions, and its rational manipulation *in vitro* was feasible with a deeper understanding of the parameters that influenced it. It's not the scope of this paper to have all the answers on how SbpA self-assemble in the surface of the bacterial cell after protein secretion. We are aware of the complexity of the system, and the limitations of analyzing SbpA self-assembly in solution, as the interactions of SbpA with the SCWP in the bacterial surface are not being considered in the present study.

MATERIAL AND METHODS

Reagents and other chemicals

All aqueous solutions were prepared using reagent grade (18 MΩ cm resistivity) deionized water (DI H_2O) purchased from Stephens Scientific Co. (Riverdale, NJ). Unless stated otherwise, all other reagents and chemicals (ACS grade or better) were purchased either from Aldrich Chemical Co. (Milwaukee, WI) or from Sigma Chemical Co. (St. Louis, MO) and were used as received.

Purification of SbpA

The bacterial cell surface layer protein (SbpA) was isolated from *Lysinibacillus sphaericus* (American Type Culture Collection No. 4525). *L. sphaericus* was grown at 30 ^{o}C in nutrient broth containing 11.1 mM glucose, 7.46 mM K_2HPO_4, and 0.4 mM $MgSO_4$. Upon reaching an optical density between 0.5 and 0.6 at 600 nm, the cells were then harvested by centrifugation at 16,000 x *g* for 20 min at 4 ^{o}C. After the first centrifugation step, the cells were washed three times by repeated resuspension/centrifugation at 16,000 x *g* in 50 mM sodium phosphate buffer (pH 7.4). After the washing steps, the pellet was resuspended in a 10-fold volume of Buffer A (50 mM Tris-Cl pH 7.2, 5 M guanidine hydrochloride), stirred for 20 min at room temperature, and centrifuged at 40,000 x *g* for 30 min at 10 ^{o}C. The supernatant containing the SbpA monomeric subunits was collected and centrifuged again at 40,000 x *g* for 30 min at 10 ^{o}C (2 times). The cleared supernatant containing the SbpA monomers was subjected to size exclusion chromatography using a Superdex 200 Column (GE Healthcare) equilibrated with Buffer A. Fractions containing SbpA were pooled and dialyzed against Buffer B (50 mM Tris pH 7.8, 1mM EDTA). Finally, the solution of purified SbpA was adjusted to give a protein stock concentration of ~ 5 μM in Buffer B, and stored at 4 ^{o}C. 1 mM EDTA was shown to increase the stability of the protein stock, when checked by DLS for the presence of aggregates. Protein purity was assessed by SDS-PAGE, stained with SimplyBlue^{TM} Safestain from Invitrogen^{TM} (Carlsbad, CA) following the manufacturer's instructions.

All buffer stock solutions were filtered through a nylon membrane (0.22 μm) after preparation and stored at 10 ^{o}C. Samples for the protein self-assembly reactions were prepared by diluting a desired amount of protein stock solution (5 μM SbpA) to a volume of 100 μL with buffer B (50 mM Tris pH 7.8, 1 mM EDTA). Calcium chloride was added at the desired concentration for the assembly reaction initiation from a 1 M

stock solution, right after the volume was adjusted with DI H_2O to reach 300 μL total final volume when Calcium chloride was added.

The self-assembly of SbpA in solution was primarily monitored in real-time by dynamic light scattering (DLS) measurements immediately after the mixture of the reagents. The DLS measurements were carried out using a Zetasizer Nano ZS instrument (Malvern Instruments, UK). The Z-average (cumulants mean) diameter was used for all DLS kinetic analyses, where each reported diameter value is averaged over 10 measurements (with a 10-second acquisition time for each measurement). The reported Z-average values used for the kinetic analysis are the average of two independent measurements. The Z-average diameter and the calculated diameter of the molecules expressed by the number of molecules present in solution were calculated using the Dispersion Technology software version 5.1 (Malvern Instruments, UK). To determine the monomer diameter, the protein stock solution was diluted to 2324.1 nM in buffer B to a volume of 100 μL, and the final volume adjusted to 300 μL with DI H_20. The results were expressed by the percentage of populations present by number in the sample, and were calculated using the Dispersion Technology software version 5.1.

The self-assembly of SbpA was also monitored in real-time by taking optical density (absorbance) measurements at 380 nm wavelength using a Molecular Devices (Sunnyvale, CA) Spectramax Plus^{384} spectrophotometer plate reader instrument. Optical density (O.D.) measurements were recorded by the spectrophotometer software every minute for ~ 4 h. Before each reading, the sample was automatically agitated for 5 seconds by the equipment. The reported O.D. values used for the kinetic analysis are the average of three measurements.

The rate constants for the first 20 minutes, expressed as *k,* was determined from the slopes of linear fits calculated using OriginPro 7.5. The first 20 minutes of

data were empirically chosen for calculating the rate constant because of the low degree of scatter observed during the initial phase of the self-assembly reaction when compared to the latter phases. The Arrhenius plot, and the thermodynamic parameters were calculated from the slopes of the temperature dependence on the assembly kinetics as described by Wilson & Benight (38).

Electron Microscopy

The self-assembled protein samples were visualized using a Morgagni 268 transmission electron microscope (Philips/FEI Company, Hillsboro, OR) operated at an accelerating voltage of 80 kV. After four hours of *in vitro* reassembly at the same conditions used for the kinetic analysis, droplets of the samples were placed into Petri dish, and 200-mesh carbon-coated Formvar copper TEM grids from Electron Microscopy Sciences (Hatfield, PA) were put in contact with the sample for 30 minutes for adsorption. Prior to imaging, the samples were negatively stained for 30 seconds with a methylamine tungstate stain from Nanoprobes (Yaphank, NY), and rinsed twice in a droplet of DI H_2O.

Fourier Transform Analysis.

To facilitate qualitative examinations of the assembled products, , TEM micrographs (512 × 512 pixels) were processed using the 2-D fast Fourier transform (FFT) algorithm (39) in the Digital Micrograph software program (Gatan, CA). In this procedure, masking pattern (with edges smoothed over 5 pixel units) was applied on the intense spots of the FFT power spectrum. An enhanced, noise-filtered image was subsequently obtained by performing an inverse FFT operation (40) on the masked power spectrum.

RESULTS AND DISCUSSION

The purity of the protein used in the kinetic studies was checked by SDS-PAGE (Inset Figure 2.1). The initial protein solution was also checked by DLS. Figure 2.1 shows the average diameter distribution by the percentage of the number of molecules present. As shown in Figure 2.1, the main population of SbpA molecules in solution has a diameter close to 9.0 nm. This diameter is approximately the expected diameter of a globular protein of 129 kDa, 9.5 nm, which is the molecular weight of SbpA. This result demonstrated that the initial preparation of purified SbpA solution used in this study was mainly composed of monomers. This initial characterization by DLS was used for the optimization of SbpA purification, and was routinely used to check every new purified SbpA sample prior to each experiment. We could observe the formation of aggregates when the protein was stored for more than three weeks when EDTA was absent in the stock solution. However, when 1 mM of EDTA was added to the protein stock, SbpA monomers remained stable for longer periods, and small protein aggregates were not observed until after two months of storage at 4 °C. The influence of protein concentration on SbpA self-assembly was investigated by DLS in the presence of 45 mM $CaCl_2$. Each data point shown on Figure 2.2a corresponds to the Z-average diameter obtained from the DLS measurements and is plotted as a function of time. The Z-average diameter is defined as the intensity weighted mean average for the ensemble collection of particles in the sample derived from the slope of the linearized form of the correlation function. As the light scattering signal intensity is proportional to the square of the molecular weight, it is very sensitive to subtle changes in the oligomeric state of the protein.

Even though monomers are the majority of the molecules initially present in solution, as observed in the plot with the average diameter by the percentage of the different molecule populations (Figure 2.1), the initial Z-average diameter of ~ 75 nm

reflects the sensitivity of the Z-average for the presence of oligomeric states of SbpA in solution. This diameter was not even observed when the result was expressed by percentage of number of molecules as seen in Figure 2.1.

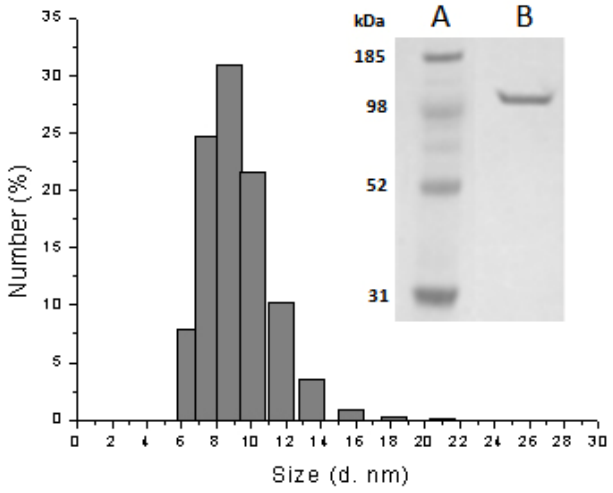

Figure 2.1. Size distribution of SbpA calculated by DLS. Results expressed by percentage of the number of molecules. Inset: SDS-PAGE of SbpA. **Lane A**, MultiMark® Multi-Colored Standard; **Lane B**, 5 µL SbpA sample.

As shown in Figure 2.2c, the self-assembly reaction rate is dependent on the protein concentration present in the reaction. The rates of assembly were estimated as the slope of the Z-average diameter increase over the first 20 minutes of reaction. A lag phase was not observed or was too short to be detected in the assembly reaction by the parameters used in the DLS experiment at lower protein concentrations, up to 2324 nM. At a protein concentration of 3098 nM and above, a lag phase was observed, and the kinetic profile changed from a sigmoidal to an exponential profile as seen in Figure 2.2a. At 3873 nM, a lag phase of approximately 30 minutes is observed in the self-assembly process, and much shorter at 3098 nM. The lag phase observed at this high SbpA concentration may be due to the formation of a kinetic trap by

accumulation of an excess number of self-assembly nucleation sites. This phenomenon would be expected to delay the growth and formation of large-size crystals, which would have a correspondingly large Z-average diameter. During the lag phase observed at 3873 nM, the polydispersity index had an obvious increase reaching values as high as 0.6 (data not shown), even though the resulting Z-average diameter did not change. By the end of the lag phase, the polydispersity index had a steep decrease, reaching the levels, lower than 0.1, observed for the self-assembly experiments at lower protein concentrations (data not shown). The high polydispersity index exclusively observed may reflect the different populations of sizes present during the lag phase, as during this phase populations of monomers, nucleation sites of different sizes, as well as associated nucleation sites and larger polymers could be present and in formation in solution. However, the steep drop in the polydispersity index previous to substantial increase in the Z-average diameter possibly indicates that larger polymers were not very abundant in the reaction, and that the initial increase in the polydispersity index be due mainly by the presence of monomers and nucleation sites being formed. If larger polymers were present during the lag phase, when the polydispersity index had the decrease to levels in which the DLS data is more trustful, this would have a direct impact in the final Z-average diameter, what was not observed. A polycrystalline array was observed by TEM when the assembly was performed at high protein concentrations, Figure 2.3b and 2.3c, and a monocrystalline array when the assembly was performed at 2324 nM SbpA Figure 2.3a. The polycrystalline array observed corroborates with the kinetic trap observed by the formation of an excess of nucleation sites. At a protein concentration of 3098 nM, the assembly rate observed was approximately 2-fold lower than the rate obtained in the presence of 3873 nM SbpA. Similar examples of kinetic traps in protein self-assembly reactions at high protein concentrations were also observed in other systems (41-43).

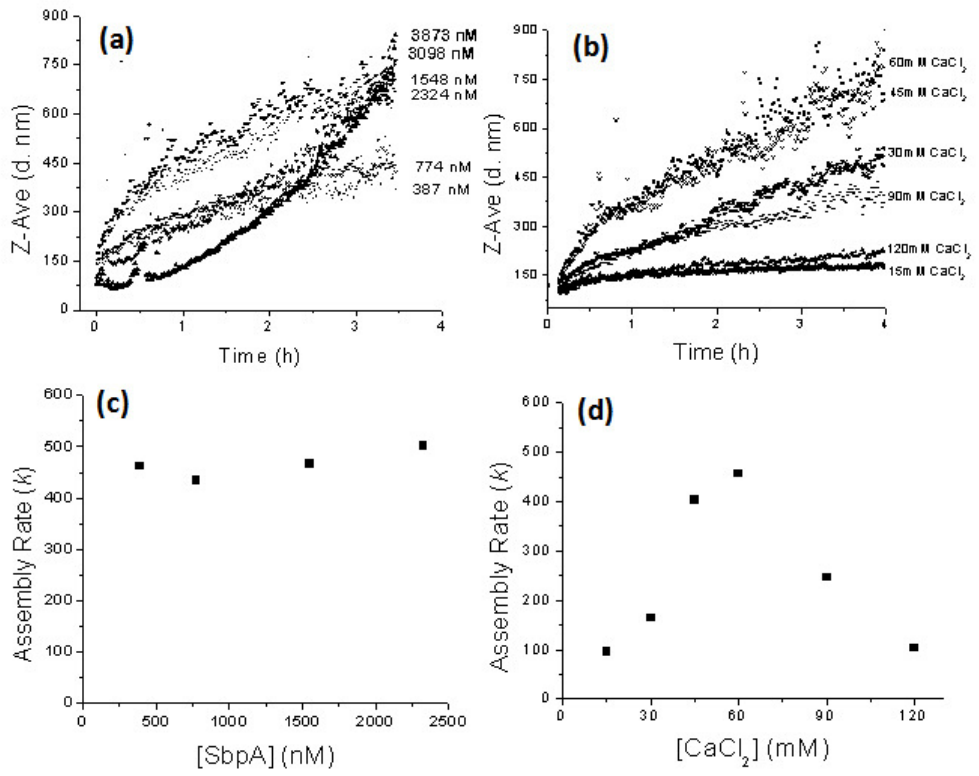

Figure 2.2. (**a**) Kinetics of SbpA self-assembly monitored by DLS under different protein concentrations (387.3 nM -3873.5 nM), and at a constant calcium concentration of 45 mM. (**b**) Kinetics of SbpA self-assembly monitored by DLS under different calcium concentrations (15-120 mM), and at a constant protein concentration of 2324 nM. All the self-assembly reactions were performed at 35 ^{o}C. Dependence of protein concentration ([SbpA] - nM), (**c**), and calcium chloride concentration ([$CaCl_2$] – mM (**d**) on the assembly rate *k* of the kinetics of SbpA self-assembly. The assembly rate was calculated from the slope of a linear fit from the first 20 minutes of the kinetics of SbpA Self-assembly from (a) and (b) for the effect of protein and calcium concentration respectively using OriginPro 7.5.

The possible kinetic trap observed at high protein concentrations is normally caused by the formation of a vast number of multiple nucleation points for self-assembly, and consequently the formation of S-layer recrystallized products that are ultimately polycrystalline in nature rather than single-crystalline, as confirmed by transmission electron microscopy (Figure 2.3a-c). Polycrystalline S-layers form because the assembly of the monomers at each nucleation site proceeds until it randomly meets the boundary of another crystalline domain. When the boundaries of two or more growing crystalline domains come into contact, the adjacent sites for the incorporation of new monomers become buried, and further assembly at those points ceases. Although polycrystalline types of S-layer matrices provides a configuration with a minimum free energy condition, they are generally not viewed as being ideal for certain nanobiotechnological applications (27-29) in which a monocrystalline domain would be more beneficial (e.g., the creation of long-range ordered periodic arrays of nanoparticles for studying the collective optoelectronic effects of nanoscale ordering).

Previous studies conducted by Pum and Sleytr have suggested that calcium ions are essential for the self-assembly of SbpA, and that the concentration of this ion is a critical parameter that determines the shape and size of the recrystallized S-layer lattices (44). However, although calcium appeared to be essential for the self-assembly of SbpA as well as for many other S-layers, there is currently no data showing how calcium ions specifically affect SbpA assembly kinetics. In general, metal ions can potentially play multiple roles in protein self-assembly. For example, the weak association of calcium ion(s) with SbpA might be directly involved in its assembly mechanism via one or more of the following mechanisms: (1) calcium may bind to a specific site of the protein, thereby modifying the structure and consequently exposing one or more protein domain(s) required for the assembly process; (2) calcium may be

involved in the formation of calcium-mediated interactions between the protein subunits; and/or (3) calcium may function to neutralize negative charges within domains involved in the assembly reaction, thereby facilitating the self-assembly process. The influence of calcium on the kinetics of SbpA self-assembly was investigated here in greater detail by DLS. Figure 2.2b shows the assembly of SbpA over a time course of ~ 4.0 h under different concentrations of $CaCl_2$. The data shown clearly demonstrate that SbpA undergoes self-assembly at a rate that is dependent on calcium concentration. Over the range of calcium concentrations investigated here (15-120 mM $CaCl_2$), SbpA self-assembly showed the same sigmoidal kinetic profile as the one observed at lower protein concentration. Similarly, no detectable lag phase was observed on the time scale of the experiment and an apparent increase in the Z-average diameter could be detected immediately after the addition of calcium chloride to the reaction. Figure 2.2c and 2.2d show the effect of protein concentration and the effect of calcium concentration respectively on the rate of SbpA self-assembly *in vitro*. Figure 2.2c shows that when the concentration levels of protein are < 2324 nM, k changes only slightly even with a 4-fold increase in protein concentration. In contrast, k is quite sensitive to changes in calcium concentration (Figure 2.2d), whereas a 5-fold increase in k is observed with a 4-fold increase in calcium concentration (from 15-60 mM $CaCl_2$). A maximum value of k is attained at 60 mM $CaCl_2$ under the protein concentration used (i.e., 2324 nM SbpA), and undergoes a marked reduction upon increasing the calcium concentration above 60 mM. When the calcium concentration approaches 120 mM, k is reduced to values similar to the ones observed at 15 mM $CaCl_2$. At 15 mM, and 120 mM of Calcium chloride in the reaction, just small patches of assembled product could be observed in the sample when checked by TEM (Data not shown). The observed decrease in the assembly rate above 60 mM of $CaCl_2$ may be caused by one or more of the following reasons: 1) calcium ions are bound to every

available binding site on each monomeric unit of SbpA, and therefore the formation of calcium-mediated interactions between the protein subunits is prevented; or 2) the calcium ions cause the charge density distribution around the protein monomers to increase to a level at which the subunits repel each other, and therefore the rate of self-assembly is reduced or the process is prevented from occurring altogether.

In order to obtain information about the thermodynamics of S-layer recrystallization, the effect of temperature on the self-assembly of SbpA was also analyzed. Figure 2.4a shows the dependence of SbpA self-assembly reaction on temperature. The kinetic profile observed for the temperature range tested here was similar to the ones observed at low protein concentration and at different calcium chloride concentrations. By observing the assembly rate for the first 20 minutes of reaction (Figure 2.4b), it is clear that *k* initially increases with a rise in temperature, reaching a maximum value at around 45 ^{o}C, but then a further increase in temperature caused a decrease in the assembly rate. The increase in the assembly rate as a function of temperature demonstrates that SbpA self-assembly is an entropy-driven process determined solely by its amino acid sequence, in agreement with the results observed previously by Jaenicke and co-workers for the S-layer protein of *B. stearothermophilus* (35).

For a quantitative evaluation of the activation thermodynamics, an Arrhenius plot (Figure 2.4c) was calculated using the data from Figure 2.4b. The obtained value of the activation energy (81.6 kj mol^{-1}) reflects the high degree of sensitivity of SbpA self-assembly to temperature. A loss of linearity in the Arrhenius plot for temperatures of 35 ^{o}C and higher is observed. This loss of linearity could be caused by a modification in the monomers to a state that is unfavorable for polymerization. This observation is similar to those reported for other protein self-assembly systems (38, 45), and is also in agreement with the results obtained for the *B. stearothermophilus* S-

layer (35), wherein nonspecific aggregation of denatured protein was observed at temperatures above 35 ^{o}C.

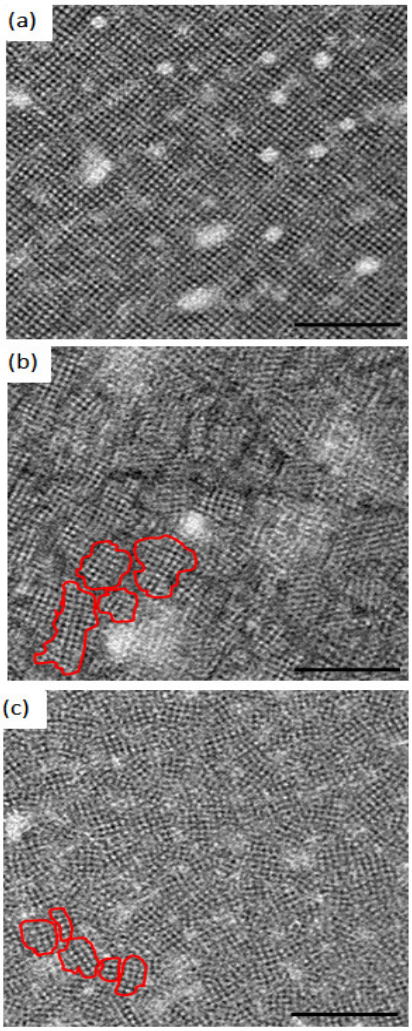

Figure 2.3. Noise-filtered inverse FFT Brightfield TEM (negative-stain) images of native self-assembled SbpA. (a) 2324.1 nM SbpA and 45 mM $CaCl_2$, (b) 3098.8 nM SbpA and 45 mM $CaCl_2$, and (c) 3873.5 nm SbpA and 45 mM $CaCl_2$. The self-assembly reactions were performed at 35 ^{O}C. Scale bar = 100 nm. For easier visualization, a few single crystals, and its adjoining parts were manually marked in red in (b), and in (c).

Here, although the maximum observed rate of assembly of SbpA as determined by DLS occurs at 45 ^{o}C, the apparent rate at this temperature may be associated with nonspecific aggregation of denatured SbpA monomers. To reinforce this idea, assembled products could be observed at 35 ^{o}C by TEM, and clear assembled product could not be observed when the self-assembly reaction was performed at 45 ^{o}C and above (Data not shown). Unfortunately, DLS does not permit the discrimination between self-assembled recrystallization products and nonspecific aggregation products; it only measures the size/diameter of whatever component species may be present in a given system, which makes essential for each experiment the observation of the final assembled product by TEM. In any case, the observed temperature dependence demonstrates that SbpA self-assembly is an endothermic process that is highly sensitive to temperature.

A plausible explanation for the observed increase in the SbpA self-assembly rate with increasing temperature is that entropically favorable hydrophobic interactions probably play an important role in mediating the protein-protein interactions necessary for self-assembly. The high value for the activation entropy calculated from the Arrhenius plot (129.34 J mol^{-1} K^{-1}) supports this possibility.

When the temperature is increased, the SbpA monomers interact with each other by hydrophobic surfaces interactions to form the S-layer array. These interactions happen with the simultaneous release of entropically disfavored water molecules of the hydration layer surrounding the hydrophobic domains in the protein. These solvating water molecules which are released during protein self-assembly provide the increase in entropy necessary to drive the self-assembly process forward. Even though SbpA self-assembly occurs with the resultant formation of a highly regular structure, thus causing a local decrease in entropy, the net entropy of the system is ultimately increased as a result of the increased degrees of freedom experienced by the large

number of water molecules released from the hydration shell formed on the surface of the hydrophobic domains of the interacting protein molecules. A similar behavior is also observed in other entropy-driven biological self-assembly systems (46-49).

The overall entropy change during SbpA assembly can be partitioned into two components, namely, the protein entropy and the water entropy. Whereas the water entropy corresponds to the entropy change due to water release from the protein interface during the assembly process, the protein entropy is the change associated with the incorporation of protein molecules into the S-layer lattice. The value of the protein entropy is typically much smaller in magnitude when compared to the water entropy. Therefore, the large positive value of the activation entropy (129.34 J mol^{-1} K^{-1}) calculated for the self-assembly of SbpA is mainly due to the entropy gain arising from the release of a large number of water molecules associated with the SbpA monomers prior to the assembly process minus the protein loss of entropy. The positive calculated activation enthalpy (120.81 kJ mol^{-1}) for SbpA self-assembly also provides supporting evidence that the assembly process is accompanied by a net loss of hydrophobic surfaces, as positive values of entropy and enthalpy are characteristic of reactions in which a net loss of hydrophobic surfaces is observed (46).

To obtain more detailed mechanistic information about how SbpA S-layers undergo self-assembly in vitro, the ionic strength effect on SbpA self-assembly was tested by performing the self-assembly reaction in the presence of different concentrations of sodium chloride. The self-assembly process was monitored by measuring the increase in optical density at 380 nm, which was chosen based on empirical wavelength scans of free SbpA monomers as compared to 2D S-layer assemblies.

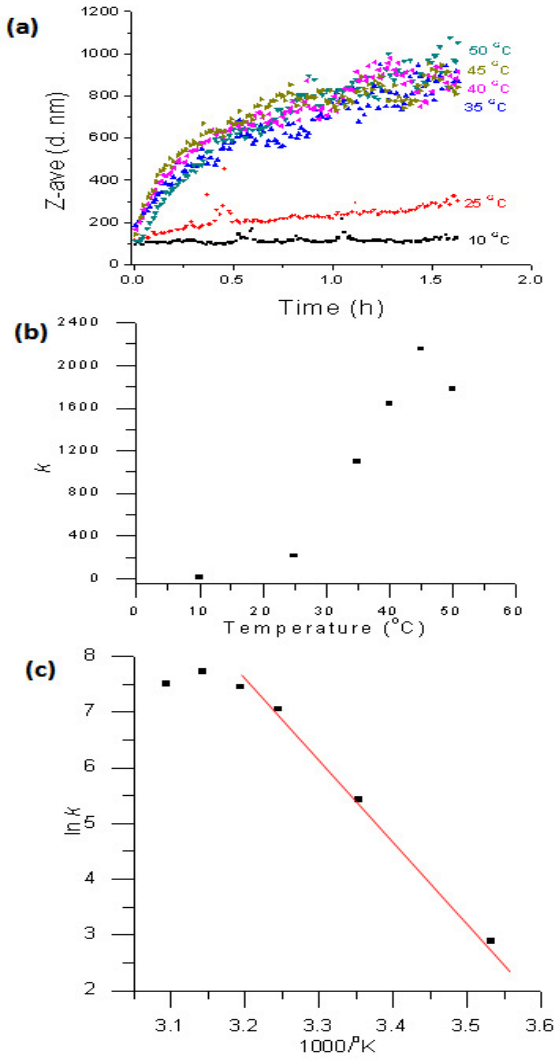

Figure 2.4. (a) Kinetics of SbpA self-assembly monitored by DLS under different temperatures (10 – 55 ^{O}C). For all curves, the calcium concentration is 45 mM, and the protein concentration is 2324.1 nM. (b) Temperature dependence of the rate of the kinetics of SbpA self-assembly. (c) Arrhenius plot for the kinetic rate of SbpA self-assembly calculated from the data shown in (b). The Arrhenius plot was calculated using the method described by Wilson & Benight.[38]

From the wavelength scan results, it was found that at 380 nm SbpA monomer absorption is negligible and for newly formed 2D assemblies not. The assembly kinetics rate, *k,* was also calculated from the slopes of a linear fit of the first 20 minutes of the kinetic assembly curves shown in Figure 5a The measured *k* at NaCl concentration levels <10 mM remained approximately constant, as seen in Figure 5b. A 50 % decrease in the assembly rate, however, was observed when the NaCl concentration was increased from 10 mM to 20 mM; and a further 30 % decrease in the assembly rate was observed with a subsequent increase in NaCl levels to 40 mM. The decreasing trend in *k* with increasing ionic strength is different from the increase in the assembly reaction of some virus capsid, in which repulsive Coulomb interactions between the coat proteins resulting from the presence of a net electrical charge on them are at certain level neutralized (50). A plausible reason for the decreasing trend observed for SbpA self-assembly may be caused by a decrease in the interaction of calcium (which has been shown here to be an essential component in the assembly process) with the SbpA monomers when in the presence of a high ionic strength. Alternatively, this monotonic decrease in the rate of SbpA self-assembly with increasing buffer ionic strength could also be due to a decrease in electrostatic interactions that could be also a contributing factor in the self-assembly process.

By studying the SbpA self-assembly mechanism under different conditions in solution, it was shown that SbpA undergoes self-assembly at a rate that is dependent on the protein concentration, temperature, and different environmental conditions (i.e., presence/concentration of, calcium, and NaCl). By varying the protein concentration, we could control the formation of polycrystalline versus larger monocrystalline arrays of SbpA in solution.

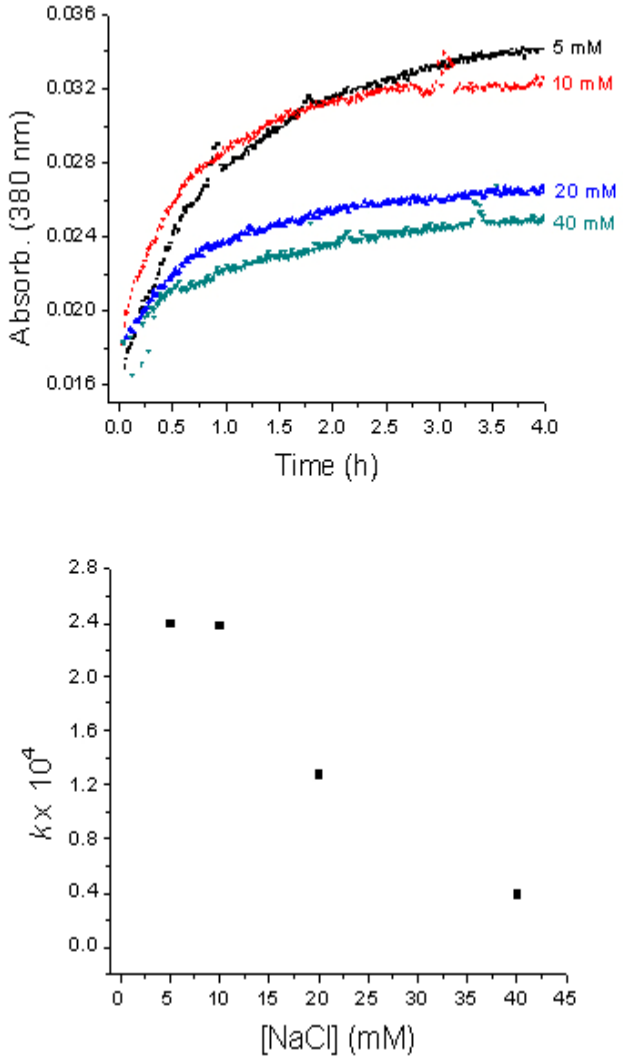

Figure 2.5. (a) Kinetics of SbpA self-assembly monitored by absorption spectrophotometry at 380 nm under different sodium chloride concentrations (5 -40 mM). For all curves, the self-assembly was performed at 35 ^{O}C, the calcium concentration is 45 mM, and the protein concentration is 2324.1 nM. (b) Calcium chloride dependence of the rate (k) of the kinetics of SbpA self-assembly.

The formation of polycrystalline arrays was generally favored in the presence of high protein concentrations. The data from the kinetics of SbpA self-assembly under the influence of different temperatures implies that this process is entropically driven, and that a net loss of hydrophobic surfaces likely occurs when the SbpA monomeric units are incorporated into the S-layer array. We have also shown that the presence of calcium is necessary for the assembly process; however at high calcium concentrations, the self-assembly rate is dramatically reduced and just small patches of assembled product could be observed by TEM, indicating a deleterious effect of calcium chloride at this levels. This study helps to understand the influence of the different parameters tested here on the interaction of SbpA monomers during SbpA self-assembly, and these finding can thereby facilitate the rational manipulation and optimization of this process for future nanobiotechnological applications.

REFERENCES

1. Casini, G. L., D. Graham, D. Heine, R. L. Garcea, and D. T. Wu. 2004. In vitro papillomavirus capsid assembly analyzed by light scattering. Virology, 325:320-327.

2. Gonzalez, J. M., M. Velez, M. Jimenez, C. Alfonso, P. Schuck, J. Mingorance, M. Vicente, A. P. Minton, and G. Rivas. 2005. Cooperative behavior of Escherichia coli cell-division protein FtsZ assembly involves the preferential cyclization of long single-stranded fibrils. Proc. Natl. Acad. Sci. U. S. A., 102:1895-1900.

3. Mach, H., D. B. Volkin, R. D. Troutman, B. Wang, Z. Luo, K. U. Jansen, and L. Shi. 2006. Disassembly and reassembly of yeast-derived recombinant human papillomavirus virus-like particles (HPV VLPs). J. Pharm. Sci., 95:2195-2206.

4. Paintsil, J., M. Muller, M. Picken, L. Gissmann, and J. Zhou. 1998. Calcium is required in reassembly of bovine papillomavirus in vitro. J. Gen. Virol., 79:1133-1141.

5. Van Hest, J. C., and D. A. Tirrell. 2001. Protein-based materials, toward a new level of structural control. Chem. Commun., 19:1897-1904.

6. Sara, M., and U. B. Sleytr. 2000. S-Layer proteins. J. Bacteriol., 182:859-868.

7. Sotiropoulou, S., Mark, S.S., Angert, E.R., and Batt, C.A. 2007. Nanoporous S-Layer Protein Lattices. A Biological Ion Gate with Calcium Selectivity. J. Phys. Chem. C, 111:13232 - 13237.

8. Messner, P., D. Pum, M. Sara, K. O. Stetter, and U. B. Sleytr. 1986. Ultrastructure of the cell envelope of the archaebacteria Thermoproteus tenax and Thermoproteus neutrophilus. J. Bacteriol., 166:1046-1054.

9. Baumeister, W., and G. Lembcke. 1992. Structural features of archaebacterial cell envelopes. J. Bioenerg. Biomembr., 24:567-575.

10. Dooley, J. S., W. D. McCubbin, C. M. Kay, and T. J. Trust. 1988. Isolation and biochemical characterization of the S-layer protein from a pathogenic Aeromonas hydrophila strain. J. Bacteriol., 170:2631-2638.

11. Ilk, N., C. Vollenkle, E. M. Egelseer, A. Breitwieser, U. B. Sleytr, and M. Sara. 2002. Molecular characterization of the S-layer gene, sbpA, of Bacillus sphaericus CCM 2177 and production of a functional S-layer fusion protein with the ability to recrystallize in a defined orientation while presenting the fused allergen. Appl. Environ. Microbiol., 68:3251-3260.

12. Jakava-Viljanen, M., and A. Palva. 2007. Isolation of surface (S) layer protein carrying Lactobacillus species from porcine intestine and faeces and characterization of their adhesion properties to different host tissues. Vet. Microbiol., 124:264-273.

13. Wang, B., E. Kraig, and D. Kolodrubetz. 1998. A new member of the S-layer protein family: characterization of the crs gene from Campylobacter rectus. Infect. Immun., 66:1521-1526.

14. Avall-Jaaskelainen, S., and A. Palva. 2005. Lactobacillus surface layers and their applications. FEMS Microbiol. Rev., 29:511-529.

15. Gyorvary, E. S., O. Stein, D. Pum, and U. B. Sleytr. 2003. Self-assembly and recrystallization of bacterial S-layer proteins at silicon supports imaged in real time by atomic force microscopy. J. Microsc., 212:300-306.

16. Huber, C., J. Liu, E. M. Egelseer, D. Moll, W. Knoll, U. B. Sleytr, and M. Sara. 2006. Heterotetramers formed by an S-layer-streptavidin fusion protein and core-streptavidin as a nanoarrayed template for biochip development. Small, 2:142-150.

17. Jarosch, M., E. M. Egelseer, C. Huber, D. Moll, D. Mattanovich, U. B. Sleytr, and M. Sara. 2001. Analysis of the structure-function relationship of the S-layer protein SbsC of Bacillus stearothermophilus ATCC 12980 by producing truncated forms. Microbiology, 147:1353-1363.

18. Pleschberger, M., A. Neubauer, E. M. Egelseer, S. Weigert, B. Lindner, U. B. Sleytr, S. Muyldermans, and M. Sara. 2003. Generation of a functional monomolecular protein lattice consisting of an s-layer fusion protein comprising the variable domain of a camel heavy chain antibody. Bioconjug. Chem., 14:440-448.

19. Pleschberger, M., D. Saerens, S. Weigert, U. B. Sleytr, S. Muyldermans, M. Sara, and E. M. Egelseer. 2004. An S-layer heavy chain camel antibody fusion protein for generation of a nanopatterned sensing layer to detect the prostate-specific antigen by surface plasmon resonance technology. Bioconjug. Chem., 15:664-671.

20. Toca-Herrera, J. L., R. Krastev, V. Bosio, S. Kupcu, D. Pum, A. Fery, M. Sara, and U. B. Sleytr. 2005. Recrystallization of bacterial S-layers on flat polyelectrolyte surfaces and hollow polyelectrolyte capsules. Small, 1:339-348.

21. Schaffer, C., and P. Messner. 2005. The structure of secondary cell wall polymers: how Gram-positive bacteria stick their cell walls together. Microbiology, 151:643-651.

22. Ahsan, M. M., T. Kimura, S. Karita, K. Sakka, and K. Ohmiya. 1996. Cloning, DNA sequencing, and expression of the gene encoding Clostridium thermocellum cellulase CelJ, the largest catalytic component of the cellulosome. J. Bacteriol., 178:5732-5740.

23. Brechtel, E., and H. Bahl. 1999. In Thermoanaerobacterium thermosulfurigenes EM1 S-layer homology domains do not attach to peptidoglycan. J. Bacteriol., 181:5017-5023.

24. Engelhardt, H., and J. Peters. 1998. Structural research on surface layers: a focus on stability, surface layer homology domains, and surface layer-cell wall interactions. J. Struct. Biol., 124:276-302.

25. Mesnage, S., E. Tosi-Couture, M. Mock, and A. Fouet. 1999. The S-layer homology domain as a means for anchoring heterologous proteins on the cell surface of Bacillus anthracis. J. Appl. Microbiol., 87:256-260.

26. Tang, J., A. Ebner, N. Ilk, H. Lichtblau, C. Huber, R. Zhu, D. Pum, M. Leitner, V. Pastushenko, H. J. Gruber, U. B. Sleytr, and P. Hinterdorfer. 2008. High-affinity tags fused to s-layer proteins probed by atomic force microscopy. Langmuir, 24:1324-1329.

27. Mark, S. S., M. Bergkvist, P. Bhatnagar, C. Welch, A. L. Goodyear, X. Yang, E. R. Angert, and C. A. Batt. 2007. Thin film processing using S-layer proteins: biotemplated assembly of colloidal gold etch masks for fabrication of silicon nanopillar arrays. Colloids Surf. B Biointerfaces, 57:161-173.

28. Mark, S. S., M. Bergkvist, X. Yang, E. R. Angert, and C. A. Batt. 2006. Self-assembly of dendrimer-encapsulated nanoparticle arrays using 2-D microbial S-layer protein biotemplates. Biomacromolecules, 7:1884-1897.

29. Mark, S. S., M. Bergkvist, X. Yang, L. M. Teixeira, P. Bhatnagar, E. R. Angert, and C. A. Batt. 2006. Bionanofabrication of metallic and

semiconductor nanoparticle arrays using S-layer protein lattices with different lateral spacings and geometries. Langmuir, 22:3763-3774.

30. Sleytr, U. B., E. M. Egelseer, N. Ilk, D. Pum, and B. Schuster. 2007. S-Layers as a basic building block in a molecular construction kit. FEBS J., 274:323-334.

31. Jing, H., J. Takagi, J. H. Liu, S. Lindgren, R. G. Zhang, A. Joachimiak, J. H. Wang, and T. A. Springer. 2002. Archaeal surface layer proteins contain beta propeller, PKD, and beta helix domains and are related to metazoan cell surface proteins. Structure, 10:1453-1464.

32. Norville, J. E., D. F. Kelly, T. F. Knight, Jr., A. M. Belcher, and T. Walz. 2007. 7A projection map of the S-layer protein sbpA obtained with trehalose-embedded monolayer crystals. J, Struct, Biol., 160, 3:313-323

33. Pavkov, T., E. M. Egelseer, M. Tesarz, D. I. Svergun, U. B. Sleytr, and W. Keller. 2008. The structure and binding behavior of the bacterial cell surface layer protein SbsC. Structure 16:1226-1237.

34. Kinns, H., and S. Howorka. 2008. The surface location of individual residues in a bacterial S-layer protein. J. Mol. Biol., 377:589-604.

35. Jaenicke, R., R. Welsch, M. Sara, and U. B. Sleytr. 1985. Stability and self-assembly of the S-layer protein of the cell wall of Bacillus stearothermophilus. Biol. Chem. Hoppe Seyler, 366:663-670.

36. Cui, Y., M. T. Bjork, J. A. Liddle, C. Sonnichsen, B. Boussert, and A. P. Alivisatos. 2004. Integration of Colloidal Nanocrystals into Lithographically Patterned Devices Nano Lett., 4:1093 - 1098.

37. T. Ohshima, H. Z. S. Y. O. K. A. T. M. M. K. N. Y. 2003. Precisely ordered quantum dot array formed using AFM lithography for all-optical electron spin quantum computers. physica status solidi (c) 0:1364-1367.

38. Wilson, D. H., and A. S. Benight. 1990. Kinetic analysis of the pre-equilibrium steps in the self-assembly of RecA protein from Escherichia coli. J. Biol. Chem., 265:7351-7359.

39. Yao, H., H. Kojima, S. Sato, and K. Kimura. 2004. Interparticle Spacing Control in the Superlattices of Carboxylic Acid-Capped Gold Nanoparticles by Hydrogen-Bonding Mediation. Langmuir, 20:10317-10323.

40. Simon, P., W. Carrillo-Cabrera, P. Formanek, C. Gobel, D. Geiger, R. Ramlau, H. Tlatlik, J. Buder, and R. Kniep. 2004. On the real-structure of biomimetically grown hexagonal prismatic seeds of fluorapatite-gelatine-composites: TEM investigations along [001]. Journal of Materials Chemistry 14:2218-2224.

41. Johnson, J. M., J. Tang, Y. Nyame, D. Willits, M. J. Young, and A. Zlotnick. 2005. Regulating self-assembly of spherical oligomers. Nano Lett. 5:765-770.

42. Zlotnick, A., J. M. Johnson, P. W. Wingfield, S. J. Stahl, and D. Endres. 1999. A theoretical model successfully identifies features of hepatitis B virus capsid assembly. Biochemistry 38:14644-14652.

43. Brenner, S. L., A. Zlotnick, and J. D. Griffith. 1988. RecA protein self-assembly. Multiple discrete aggregation states. J. Mol. Biol., 204:959-972.

44. Pum, D., and U. B. Sleytr. 1995. Anisotropic crystal Growth of the S-layer of *Bacillus sphaericus* CCM 2177 at the air/water interface. Colloids and Surfaces A: Physicochemical and Engineering Aspects, 102:99-104.

45. Kadler, K. E., Y. Hojima, and D. J. Prockop. 1988. Assembly of type I collagen fibrils de novo. Between 37 and 41 degrees C the process is limited by micro-unfolding of monomers. J. Biol. Chem., 263:10517-10523.

46. Lauffer, M. A. 1975. Entropy-driven processes in biology. Mol. Biol. Biochem. Biophys., 1-264.

47. Brenner, S. L., A. Zlotnick, and W. F. Stafford, 3rd. 1990. RecA protein self-assembly. II. Analytical equilibrium ultracentrifugation studies of the entropy-driven self-association of RecA. J. Mol. Biol., 216:949-964.

48. Ceres, P., and A. Zlotnick. 2002. Weak protein-protein interactions are sufficient to drive assembly of hepatitis B virus capsids. Biochemistry 41:11525-11531.

49. Tidor, B., and M. Karplus. 1994. The contribution of vibrational entropy to molecular association. The dimerization of insulin. J. Mol. Biol., 238:405-414.

50. Parent, K. N., S. M. Doyle, E. Anderson, and C. M. Teschke. 2005. Electrostatic interactions govern both nucleation and elongation during phage P22 procapsid assembly. Virology 340:33-45.

CHAPTER 3 - THE ROLE OF LIGAND DENSITY IN THE BINDING OF *Lysinibacillus sphaericus* S-LAYER (SbpA) PROTEINS TO CARBOHYDRATES PRESENTED ON SELF-ASSEMBLED MONOLAYERS.

To be submitted to: ACS Applied Materials & Interfaces

INTRODUCTION

The surface of many *Archaea* and *Bacteria* are decorated with a paracrystalline surface layer protein array (referred to as S-layers) formed from self-assembled monomeric proteins or glycoproteins with molecular weights that can range from 40-200 kDa. These 2-D biological nanostructures exhibit a diverse set of symmetries including oblique (p1, p2), hexagonal (p3, p6) and square symmetry (p4) (1). During microorganism growth, formation of S-layers onto the cell surface is guided by monomer synthesis and secretion, followed by the entropic assembly of the monomers into the S-layer lattice, a process that is synchronized with cell growth and division. Since the discovery of S-layer protein arrays, the fundamental understanding of the mechanism of S-layer assembly has led to many studies aimed at exploiting this process *in vitro*. Isolated S-layer protein monomers of different microorganisms have been shown to self-assemble into molecular arrays *in vitro* on solid substrates (2), liposomes (3), at air-water interface (4), and on lipid films.(4) S-layer proteins maintenance of the ability to self-assemble *in vitro*, in addition to the precise physicochemical and topological characteristics of the formed molecular array, signals the potential use of these nanostructured systems for a number of applications in nanotechnology (5-9).

In Gram-positive bacteria, S-layer proteins are non-covalently linked to the cell surface by specific interactions with the secondary cell wall polymers (SCWP), which are attached to the peptidoglycan layer. During the assembly process, after synthesis and secretion of the S-layer, monomers or small crystalline patches move along the cell surface until they reach a minimum free energy by interacting with the growing S-layer crystals neighboring the mobile monomers. This process is achieved through fine-tuned interactions between the protein monomers and the protein-SCWP surface interactions – where the protein-protein interactions normally need to be stronger than

the protein-cell surface interactions. *Bacillaceae* S-layer protein subunits anchor to the SCWP in the underlying rigid cell envelope layer of the bacteria using its N-terminal region, which has a domain named the S-layer like homology (SLH) (10). The SLH domain is one of only a few common structural components that are known to exist between the S-layers of various microorganism species, and is normally composed of 55 amino acid residues, of which 10-15 are conserved residues (11-13).

S-layer from *Lysinibacillus sphaericus* (SbpA) – previously known as *Bacillus sphaericus* - forms an array with square symmetry (p4), with a center-to-center spacing of the morphological units of 13.1 nm. The mature protein is processed from a 1268 amino acid precursor by cleavage of a 30 amino acid long signal peptide from its N-terminus (14). It has been demonstrated that SbpA recognizes the SCWP of *L. sphaericus* as an anchor site, which is known to be covalently linked to the peptidoglycan backbone (15). Surface Plasmon Resonance (SPR) data revealed the existence of three different binding sites in the SLH with different affinity levels to the SCWP. In addition to the three SLH motifs in the N-terminal part of SbpA, analysis of the SbpA sequence revealed a SLH-like motif composed of 58 amino acids that are required for reconstitution of the binding domain (16).

Several groups exploring the properties of different S-layers for technological applications have self-assembled them onto a solid substrate with immobilized SCWP. Typical solid substrates are gold surfaces that have been covalently linked to chemically modified SCWP containing thiol groups for gold binding (17). Functionalizing solid substrates with SCWP effectively mimics the bacterial cell surface, and depending on the specific microorganism, different s-layers can be assembled on the surfaces with various levels of specificity between the SCWP-S-layer pair (16). For example, the chemical composition and structure of different *Bacillaceae* SCWP have been elucidated, and a great diversity in structure is observed.

These chemical and structural differences are likely related to the range in binding affinities observed for various SCWP-S-layer pairs (for a review of Gram-positive SCWP, see Schaffer & Messner (10)). One example of SCWP which had its composition and structure determined is the one from *L. sphaericus,* that is composed of a linear chain of eight to nine repeats of a backbone disaccharide motif of N-acetyl-Mannosamine (ManNAc) and N-acetyl-Glucosamine (GlcNAc), with the ManNAc group modified with a pyruvic acid (10, 15).

Though solid substrates functionalized with SCWP can be used to mimic the S-layer anchoring mechanism of the bacterial cell surface, this strategy may not be appropriate for nanotechnological applications, where precise control over substrate homogeneity and surface topology are ideal. Toca-Herrera and collaborators (18, 19) tried to mimic the bacterial surface using different synthetic polyelectrolyte surfaces as substrate for the assembly of SbpA. In their article, SbpA recrystallized better on negatively charged polyelectrolyte multilayers than on those with positive charge, which is presumably a suitable model for the negative charges on the SCWP. The importance of mimicking the bacterial surface for the self-assembly and structural stability of SbpA was further demonstrated, as recrystallized SbpA on SCWP was shown to be more resistant to chemical denaturation (e.g., strong ethanol and acidic conditions) than SbpA on hydrophilic silicon supports (19).

Considering the need for more chemical and structurally homogeneous samples for nanotechnological applications and the observed results showing that solid substrates mimicking the natural SCWPs are more appropriate for SbpA recrystallization, here we report the synthesis and characterization of a new synthetic self-assembled monolayer (SAM). The synthesized SAMs contained different densities of a GlcNAc derivative mimicking the SCWP. The different densities of the carbohydrate were formed by the aid of a polyethyleneglycol (PEG)-terminated spacer

molecule to give mixed SAMs. The binding of SbpA to the different mixed SAMs was assessed in real time by surface plasmon resonance (SPR), and the dependence of carbohydrate density on the binding affinity of SbpA to the different SAMs was assessed.

MATERIALS AND METHODS

Reagents and other chemicals

All aqueous solutions were prepared using reagent grade (18 MΩ cm resistivity) deionized water (DI H_2O) purchased from Stephens Scientific Co. (Riverdale, NJ). Unless stated otherwise, all other reagents and chemicals (ACS grade or better) were purchased either from Aldrich Chemical Co. (Milwaukee, WI) or from Sigma Chemical Co. (St. Louis, MO).

Synthesis of Compound 1, 2, and 3

Synthetic methodologies used for the Compounds **1**, **2**, and **3** are illustrated in Figure 3.1. Compound **1** was synthesized in four steps using a published procedure (20). Compound **2** was synthesized in six steps using a similar approach from the known compound, 11-mercaptoundecyl-tri(ethylene glycol). The other half of the asymmetric compound **2** was prepared using well-established chemistry. Initially, hexaethylene glycol was converted to a monotosylate derivative using a silver(I) oxide mediated process (21). This was followed by the addition of sodium azide to furnish monoazide (**4**). Addition of **4** to 11-bromoundecene under basic conditions, followed by standard chemistry provided the azido-thiol compound **5**. Conversion of 11-mercaptoundecyl-tri(ethylene glycol) into pyridyl disulfide (**6**) was accomplished by treatment with aldrithiol-2, and finally the displacement of the corresponding

thiolpyridyl group was done with azido-thiol (**5**) forming the final unsymmetrical disulfide (**2**).

For the synthesis of compound **3** N-acetylglucosamine was converted to oxazoline (**7)** using a published procedure (22).

Purification of SbpA

The bacterial cell surface layer protein (SbpA) was isolated from *Lysinibacillus sphaericus* (American Type Culture Collection No. 4525). *L. sphaericus* was grown at 30 ^{o}C in nutrient broth containing 11.1 mM glucose, 7.46 mM K_2HPO_4, and 0.4 mM $MgSO_4$. Upon reaching an optical density (OD) at 600 nm between 0.5 and 0.6, the cells were harvested by centrifugation at 16,000 x *g* for 20 min at 4 ^{o}C. After the first centrifugation step, the cells were washed three times by repeated resuspension/centrifugation steps 16,000 x *g* in 50 mM sodium phosphate buffer (pH 7.4). After the washing steps, the pellet was resuspended in a 10-fold volume of 50 mM Tris-Cl pH 7.2, 5 M guanidine hydrochloride, mixed for 20 min at room temperature, and centrifuged at 40,000 x *g* for 30 min at 10 ^{o}C. The supernatant containing the SbpA monomeric subunits was collected and centrifuged an additional two times at 40,000 x g for 30 min at 10 ^{o}C. The cleared supernatant containing the SbpA monomers was subjected to size exclusion chromatography using a Superdex 200 Column (GE Healthcare) equilibrated with 50 mM Tris-Cl pH 7.2, 3 M guanidine hydrochloride. Fractions containing SbpA were pooled and dialyzed against DI H_2O. Finally, the solution of purified SbpA was adjusted to give a protein stock concentration of approximately 0.5 μM and stored at 4 ^{o}C. Protein purity was assessed by SDS-PAGE.

Preparation of mixed SAMs.

Stock solutions of compounds 1 and 2 in ethanol were combined at different ratios to give a final total concentration of 1 mM in ethanol (adsorption solution). The gold surface of the SPR sensor chip (Nomadics, Oklahoma City, OK) was rinsed with ethanol, and immersed in the adsorption solution for 14-16 h. After the adsorption period, the chips were rinsed with ethanol, dried with nitrogen gas, and kept at 4 ^{o}C for further use. The SPR chip containing the SAMs were then mounted into the SPR unit and the N-acetylglucosamine derivative (compound 3; carbohydrate) was conjugated *in situ* to the SAM at the azide residue in compound 2 using standard click chemistry conditions (23). Briefly, an aqueous mixture of the carbohydrate (10 mM), L-ascorbic acid (0.15 mM) and $CuSO_4$ (0.01 mM) was pumped over the SPR chip for 4 hrs. at a flow rate of 10 μL/min. The reaction of the carbohydrate with the azide in compound **2** was performed in one of the chambers of the chip. The second chamber, in which the sugar was not incorporated, was used as a reference surface, and its SPR signal subtracted from the protein-sugar interaction response of the sugar-functionalized chamber.

SPR Measurements

A SensiQ Instrument (Nomadics, Oklahoma City, OK) was used to measure the binding of SbpA to the surfaces containing different densities of carbohydrate. The stock solution of SbpA in DI H_2O was centrifuged at 16 000 x *g* for 10 minutes for removal of assembled products. The solution containing SbpA monomers was then diluted in DI H_2O and a 10X concentrated solution of the running buffer [150 mM NaCl, 10 mM HEPES, 3 mM EDTA, 0.005 % Tween 20, and 5 % Glycerol, pH 7.2) resulting in the desired final protein concentrations. Running buffer was used as a negative control, and its SPR signal subtracted from the protein-sugar interaction

response. All SPR experiments were performed at a constant flow rate of 10 µL/min with a solution of the running buffer containing the desired amount of SbpA. The association and dissociation times were equivalent for all parameters tested. For assessment of the SAM integrity, SPR experiment to measure the association of *Bandeiraea simplicifolia* BS-II lectin to the SAMs was measured and compared before and at the end of each set of SPR experiments.

RESULTS

Preparation of Mixed SAMs

Compounds 1 and 2 were diluted and mixed at different molar ratios of the carbohydrate binding molecule (compound 2). The gold substrates of the SPR chips were then submersed in the solution containing the mixture of alkanethiol-terminated molecules. Coupling the alkyne region of compound 3 to the azide group present in compound 2 of the mixed SAM was performed in the SPR instrument. After 4 hrs of reaction, the coupling of the carbohydrate was detected by a shift in the SPR profile of DI H_2O (Figure 3.3). The SPR profile of DI H_2O to demonstrate the carbohydrate coupling shown in Figure 3.3 was obtained after 10 minutes of constant flow over the sensor region of the chip, before and after the sugar coupling reaction. The SPR profile of DI H_2O at the reference chamber is also shown in Figure 3.3. The shift of the SPR profile observed after carbohydrate coupling demonstrates the successful formation of the mixed monolayer on the gold substrate. The magnitude of the shift is linearly dependent on the change in the refractive index in the interfacial region of the substrate, and consequently, in this case to the mass and amount of carbohydrate present on the substrate.

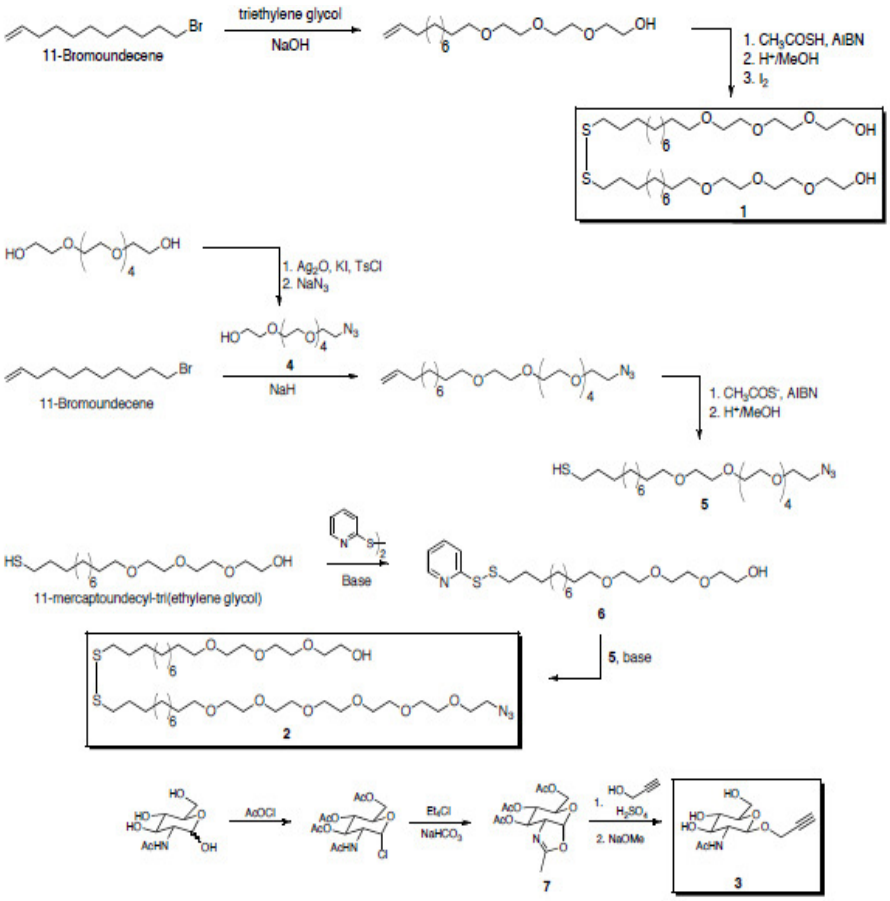

Figure 3.1. Synthesis strategies for disulfides **1** and **2**, and for alkynyl saccharide **3**. Compounds **1**, **2** and **3** *courtesy of* Aaron Strickland (Department of Food Science, Cornell University)

The coupling of the carbohydrate to the preformed mixed self-assembled monolayers was also characterized by Fourier transform infrared spectroscopy (FTIR); however, the various vibrational modes of each compound present on the SAMs could just be observed when higher carbohydrate densities were present, above 25%. At those levels, the progress of the click chemistry reaction on the mixed SAM to give the carbohydrate functionality could be monitored by the loss in the azide stretching mode at 2106 cm^{-1} (Data not shown).

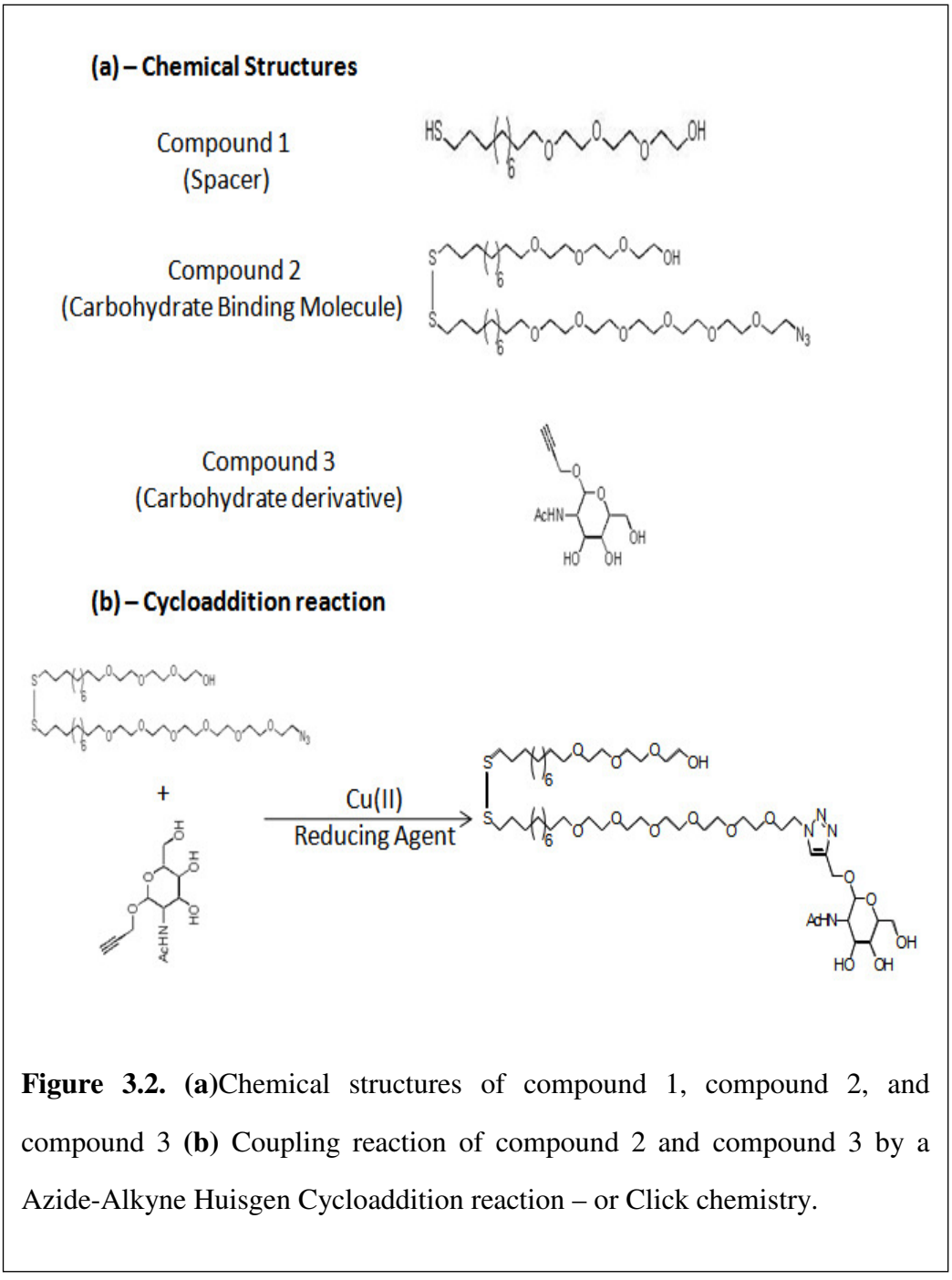

Figure 3.2. **(a)**Chemical structures of compound 1, compound 2, and compound 3 **(b)** Coupling reaction of compound 2 and compound 3 by a Azide-Alkyne Huisgen Cycloaddition reaction – or Click chemistry.

Measurement of Protein-carbohydrate Interactions at Different Ligand Densities

Prior to start the SPR experiments for measuring the binding of SbpA to the different densities of carbohydrate on the SAMs, the optimal conditions for the SPR experiments were determined (*i.e.* flow rate, association time, and surface regeneration conditions). After testing the critical parameters, the following conditions were used for all of the SPR measurements; flow rate of 10 μL/min, association time of 240 seconds, and regeneration of the surface performed by flowing 300 μL of 6 M

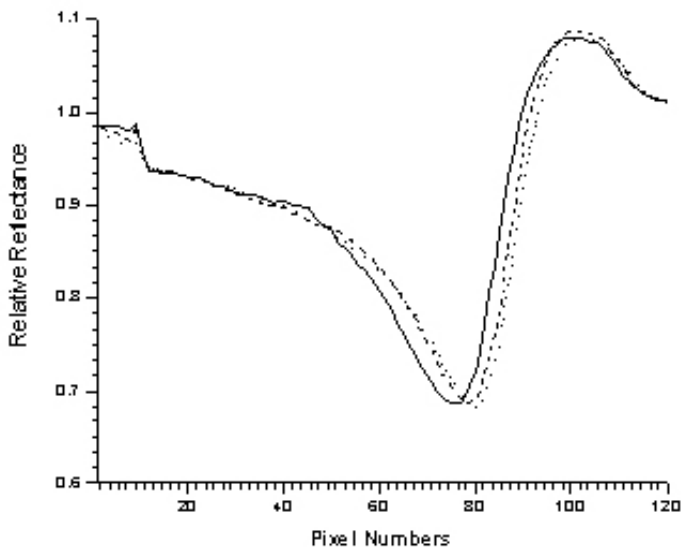

FIGURE 3.3. SPR profile of water. All the reflectance values are expressed relatively to their corresponding values in air. After carbohydrate coupling (-), reference chamber (...), and before carbohydrate coupling (--)

guanidine hydrochloride at a flow rate of 50 μL/min. During the optimization steps, the association time results showed a time dependence of SbpA: carbohydrate binding strength, as shown by the amount of protein that remained bounded to the SAMs surface, where longer times of association reaction caused a stabilization of the

complex SbpA-carbohydrate, consequently increasing the amount of protein that remained bounded to the SAM surface. A decrease of just 20% in the SPR resonance units (RU) was observed when buffer without SbpA was injected after 360 s of association reaction. However, a decrease of almost 90% in the SPR RU was observed when buffer without SbpA was injected after 120 s of association reaction, and a decrease of around 70% RU when 240 s of association reaction was used (Figure 3.4).

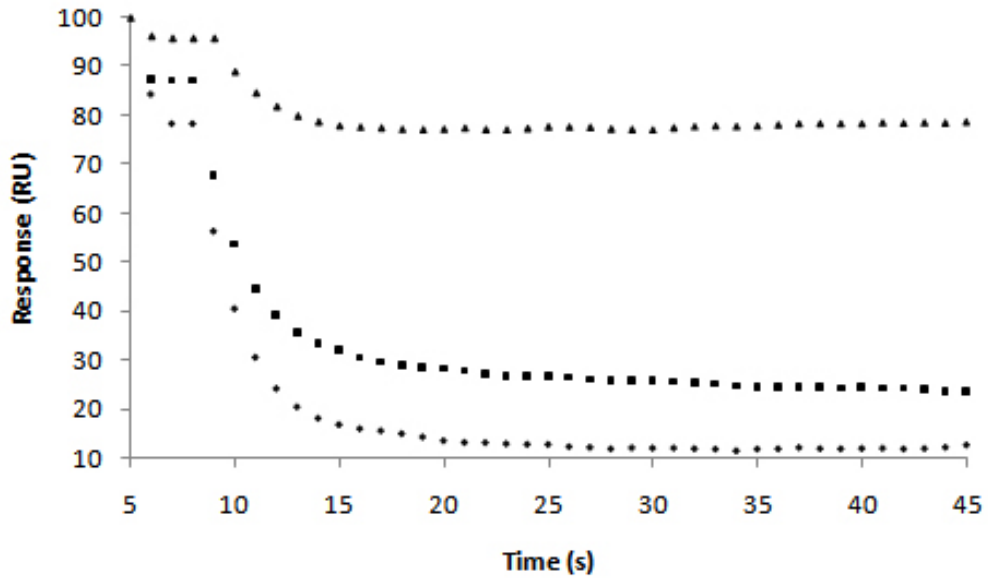

Figure. 3.4. Overlay of Normalized dissociation curves with different association times ((▲) 360s, (■) 240s, and (♦) 120s) (T_a) of a sample with 564 nM of SbpA.

The calculated dissociation rate for the three times of association reaction remained approximately constant, 2.28 +/- 0.9 s^{-1}. Normally, when reactions are independent and all the binding sites present saturated, the dissociation curves should be identical and independent of the association time. However, the change in stability of the complex protein-carbohydrate observed over time possibly indicates the presence of a linked reaction, where a two state reaction may be happening.

Figure 3.5 shows an example of SPR curves for SbpA binding to mixed SAMs containing a sugar molar ratio of 0.67 %. The dependence of carbohydrate density on the binding of SbpA to the mixed SAMs can be seen on Figure 3.6A. It shows a schematic representation of carbohydrate density effect on SbpA binding, where a

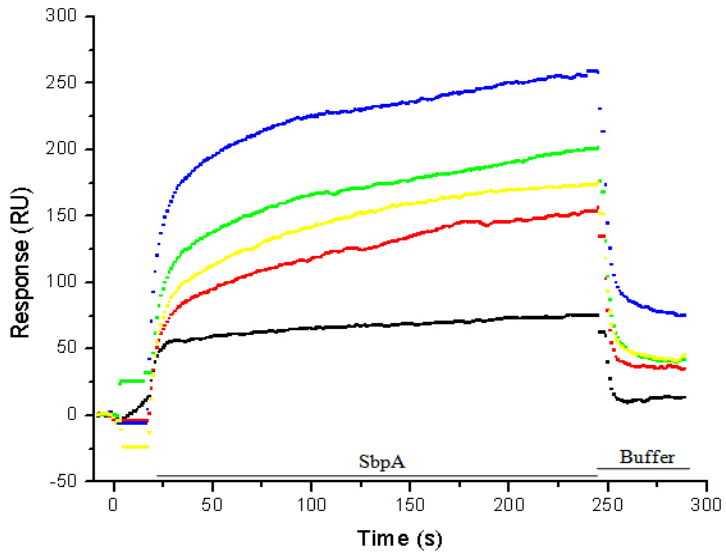

Figure 3.5. Overlaid sensograms recorded for binding of different concentrations of SbpA ; (Black) 5.64 nM, (Red) 56.4 nM, (Yellow) 141 nM, (Green) 282 nM, (Blue) 564 nM to a SAM containing 0.67 % of sugar.

higher carbohydrate density caused a decrease on protein binding. Figure 3.6B shows the relative SPR response of SbpA binding to three different carbohydrate densities, where a density of 0.67 % of carbohydrate in the SAM had higher response levels when compared to the other densities of carbohydrate tested, with a maximum SPR response of 260 SPR resonance units (RU). The maximum responses observed for both 1.72 % and 3.57% were 98.54 R.U. and 123 R.U, respectively, which are SPR responses values less than half of the ones obtained for the carbohydrate density of

0.67%. Considering one RU corresponding to approximately 1 pg mm^{-2}, and the Molecular weight of SbpA equals to 129 kDa, we estimated that with a signal of 260 RUs, 12000 SbpA molecules are immobilized on an area of 1 μm^2 of the SPR chip. If we consider the hydrodynamic diameter of SbpA to be approximately 9.5 nm, the total area occupied by all the monomers immobilized on an area of 1 μm^2 of the gold chip is equal to 0.85 μm^2, or 85% total coverage, if the protein monomers are well distributed on the surface and not stacked. With the maximum SPR response observed for the higher densities of carbohydrate on the SAMs being around 40% of the signal observed for 0.67%, this means that the estimated total protein immobilized on the SAMs of the gold chip at those density levels covers less than 50% of the surface.

DISCUSSION

Mixed SAMs containing carbohydrates were used in an attempt to mimic the components used by many *Bacillaceae* to anchor S-layers to their cell surface. The model system used here was able to answer some fundamental questions related to the binding events between SbpA and the SCWP on the bacterial cell surface. For example, in Figure 3.4 we could observe an increase in the amount of protein that remained bound to the SAMs with increasing association times. This result reflects the time dependence of the binding strength of SbpA to the carbohydrate used. This association may be caused by a conformational change of the protein upon binding to the carbohydrate, thus creating a stronger and more stable interaction, or the presence of linked interactions. The increase in the binding strength of SbpA to carbohydrate on a surface over time, as demonstrated by the increase in the amount of protein that remained bound to the SAMs with increasing association times may be an important feature for keeping the self-assembly and structure of the S-layer array on the bacterial cell surface synchronized with the cell growth and division.

If we take in consideration the amount of monomers that are necessary to cover the entire surface of an average-sized rod-shaped bacteria to be approximately $5x10^5$ monomers, and a bacteria generation time of 20 minutes, 500 molecules of S-layer would need to be synthesized and secreted per second to completely cover the bacterial cell surface (24). The slower affinity between the protein monomers and the carbohydrates of the SCWP during the first moments after protein secretion adds another level of regulation to keep the synthesis, secretion, and self-assembly synchronized. An initial weaker interaction between the protein subunits and its anchor on the bacterial cell surface would favor its mobility for reaching its low free energy arrangement when in the protein array, where the increased binding strength observed afterwards would allow the S-layer to function as a protective coat to the cell.

Figure 3.5 shows an example of the overlaid sensograms recorded from the binding of different protein concentrations to a mixed SAM that has a carbohydrate density of 0.67 %. Similar sets of experiments were carried out to investigate the influence of carbohydrate surface densities on SbpA binding. These experiments demonstrated that the binding is highly dependent on carbohydrate density (Figure 3.6). Although the interaction of proteins to monosaccharides is considered weak, K_D in the 0.1-1 mM range, monosaccharide-protein interaction can show exceptionally efficient binding due to multivalent binding effect, also known as avidity binding (25).

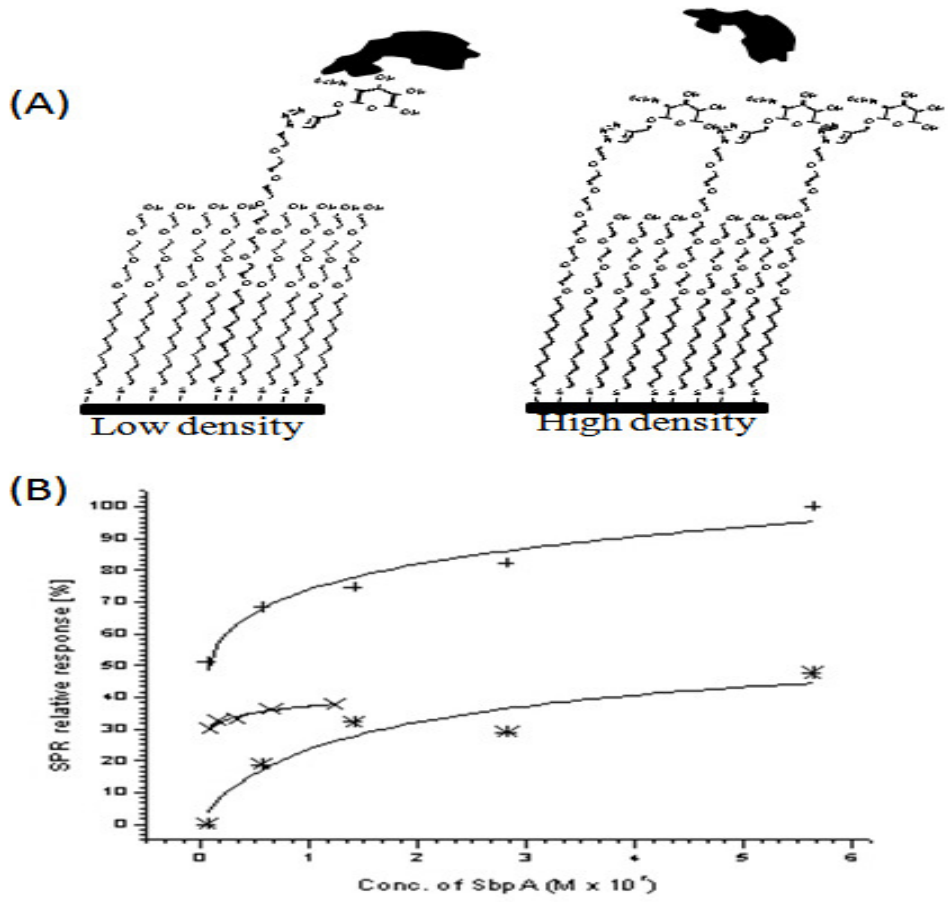

Figure 3.6. Dependence of the density of GlcNAc on the binding of SbpA to the SAMs formed on the sensor surface. (A) Schematic representation of the carbohydrate density effect on SbpA binding. (B) SPR relative binding responses measured after 240 s of injection of a solution containing 282 nM of SbpA. (+) 0.67 % of GlcNAc, (x) 1.72 % GlcNAc, (∗) 3.57 % of GlcNAc. 100% of the relative response is equal to a SPR response of approximately 260 R.U.

The avidity binding has been demonstrated to increase the protein-carbohydrate binding affinity, as well as its specificity (25). Normally, the carbohydrate density that shows the highest interaction response between the protein

and the carbohydrates on a surface is known as the critical carbohydrate density, which may reflects a dominance of polyvalent interactions. From the carbohydrate densities tested in this study, the one with the stronger binding affinity was found to be 0.67 %. At the higher carbohydrate densities tested (*i.e.* 1.72 %, and 3.57 %), a weaker affinity between SbpA and the mixed SAMs was observed. The average distance between the carbohydrates on the mixed SAMs were calculated as previously described (28). It was found that in average the lingands would be 36.1 nm apart on the 0.033% carbohydrate density SAMs, 8.02 nm apart on the 0.64% carbohydrate density SAMs, 5 nm apart on the 1.72 % carbohydrate density SAMs, and 3.47 nm apart on the 3.57 % carbohydrate density SAMs. Interestingly, the higher response was observed when the carbohydrates were in average 8.02 nm apart. The distance is very close to the calculated hydrodynamic diameter of SbpA, approximately 9.5 nm, which infers that 1:1 protein-carbohydrate interactions would be predominant. This higher response observed at this level, contradicts the increase in bind affinity normally observed by other protein-carbohydrate systems when polyvalent interactions are predominant. The decrease in binding response observed at the higher densities tested may be caused by a decrease in the physical availability of the carbohydrate within the mixed SAMs for the protein binding, which may be attributed to a steric effect that shields the protein carbohydrate binding motifs from the carbohydrates and consequently compromises the protein-carbohydrate interactions (25-27). With a carbohydrate density of 0.033 %, the binding of SbpA was similar to the binding of SbpA to the reference SPR chamber (data not shown). This decrease may be attributed to the large distances between the ligands at this density level, which were estimated to be in average 36.13 nm apart from each other. The carbohydrate density effect on the binding of SbpA suggests that this dependence may also be an important feature for keeping the self-assembly and structure of the S-layer array on

the bacterial cell surface synchronized with the cell growth and division. For example, the different carbohydrate densities could be involved in the regulation of SbpA affinity to the bacterial surface by allowing an easier migration of protein monomers or small SbpA nucleation sites at lower densities over the surface during bacterial cell growth and division. In addition, the increase in density could also allow the stabilization of the protein array. Alternatively, carbohydrate densities could also help in the establishment of SbpA-SbpA interactions during the self-assembly process by physically positioning the monomers closer together.

The real time SPR analysis of the interaction of SbpA to mixed SAMs containing the carbohydrate GlcNAc allowed us to study the influence that different carbohydrate surface densities have on SbpA binding. This is the first report that shows this influence, and the results obtained here have direct practical implications, as they demonstrate the importance of analyzing the ligand density on a surface *a priori* if the same is intended to be used as substrate for SbpA binding. Additionally, the versatility of the SAM compounds synthesized here allows the study of SbpA interaction with mixed SAMs containing other carbohydrates, such as derivatives of ManNAc, which is also present in the SCWP, or even derivatives of the disaccharide GlcNAc-ManNAc that could be used for better mimicking the SCWP. For incorporation of other carbohydrates on the SAMs, the carbohydrates derivatives would need to be synthesized with an alkyne group for coupling with the azide group present in the SAM. Our results also suggest possible routes of regulation that could be used by the bacteria to coordinate the cell wall synthesis and integrity during its growth and division.

REFERENCES

1. Sleytr, U. B., and T. J. Beveridge. 1999. Bacterial S-layers. Trends Microbiol., 7:253-260.

2. Gyorvary, E. S., O. Stein, D. Pum, and U. B. Sleytr. 2003. Self-assembly and recrystallization of bacterial S-layer proteins at silicon supports imaged in real time by atomic force microscopy. J. Microsc., 212:300-306.

3. Kupcu, S., M. Sara, and U. B. Sleytr. 1995. Liposomes coated with crystalline bacterial cells surface protein (S-layer) as immobilization structures for macromolecules. Biochim. Biophys. Acta, 1235:263-269.

4. Pum, D., M. Weinhandl, C. Hodl, and U. B. Sleytr. 1993. Large-scale recrystallization of the S-layer of Bacillus coagulans E38-66 at the air/water interface and on lipid films. J. Bacteriol., 175:2762-2766.

5. Mark, S. S., M. Bergkvist, P. Bhatnagar, C. Welch, A. L. Goodyear, X. Yang, E. R. Angert, and C. A. Batt. 2007. Thin film processing using S-layer proteins: biotemplated assembly of colloidal gold etch masks for fabrication of silicon nanopillar arrays. Colloids Surf B Biointerfaces, 57:161-173.

6. Mark, S. S., M. Bergkvist, X. Yang, E. R. Angert, and C. A. Batt. 2006. Self-assembly of dendrimer-encapsulated nanoparticle arrays using 2-D microbial S-layer protein biotemplates. Biomacromolecules, 7:1884-1897.

7. Mark, S. S., M. Bergkvist, X. Yang, L. M. Teixeira, P. Bhatnagar, E. R. Angert, and C. A. Batt. 2006. Bionanofabrication of metallic and semiconductor nanoparticle arrays using S-layer protein lattices with different lateral spacings and geometries. Langmuir, 22:3763-3774.

8. Huber, C., J. Liu, E. M. Egelseer, D. Moll, W. Knoll, U. B. Sleytr, and M. Sara. 2006. Heterotetramers formed by an S-layer-streptavidin fusion protein and core-streptavidin as a nanoarrayed template for biochip development. Small, 2:142-150.

9. Sleytr, U. B., E. M. Egelseer, N. Ilk, D. Pum, and B. Schuster. 2007. S-Layers as a basic building block in a molecular construction kit. FEBS J., 274:323-334.

10. Schaffer, C., and P. Messner. 2005. The structure of secondary cell wall polymers: how Gram-positive bacteria stick their cell walls together. Microbiology, 151:643-651.

11. Brechtel, E., and H. Bahl. 1999. In Thermoanaerobacterium thermosulfurigenes EM1 S-layer homology domains do not attach to peptidoglycan. J. Bacteriol., 181:5017-5023.

12. Mesnage, S., E. Tosi-Couture, M. Mock, and A. Fouet. 1999. The S-layer homology domain as a means for anchoring heterologous proteins on the cell surface of Bacillus anthracis. J. Appl. Microbiol., 87:256-260.

13. Engelhardt, H., and J. Peters. 1998. Structural research on surface layers: a focus on stability, surface layer homology domains, and surface layer-cell wall interactions. J. Struct. Biol., 124:276-302.

14. Ilk, N., C. Vollenkle, E. M. Egelseer, A. Breitwieser, U. B. Sleytr, and M. Sara. 2002. Molecular characterization of the S-layer gene, sbpA, of Bacillus sphaericus CCM 2177 and production of a functional S-layer fusion protein with the ability to recrystallize in a defined orientation while presenting the fused allergen. Appl. Environ. Microbiol., 68:3251-3260.

15. Ilk, N., P. Kosma, M. Puchberger, E. M. Egelseer, H. F. Mayer, U. B. Sleytr, and M. Sara. 1999. Structural and functional analyses of the secondary cell wall polymer of Bacillus sphaericus CCM 2177 that serves as an S-layer-specific anchor. J. Bacteriol., 181:7643-7646.

16. Huber, C., N. Ilk, D. Runzler, E. M. Egelseer, S. Weigert, U. B. Sleytr, and M. Sara. 2005. The three S-layer-like homology motifs of the S-layer protein SbpA of Bacillus sphaericus CCM 2177 are not sufficient for binding to the pyruvylated secondary cell wall polymer. Mol. Microbiol., 55:197-205.

17. Pleschberger, M., A. Neubauer, E. M. Egelseer, S. Weigert, B. Lindner, U. B. Sleytr, S. Muyldermans, and M. Sara. 2003. Generation of a functional monomolecular protein lattice consisting of an s-layer fusion protein comprising the variable domain of a camel heavy chain antibody. Bioconjug. Chem., 14:440-448.

18. Toca-Herrera, J. L., R. Krastev, V. Bosio, S. Kupcu, D. Pum, A. Fery, M. Sara, and U. B. Sleytr. 2005. Recrystallization of bacterial S-layers on flat polyelectrolyte surfaces and hollow polyelectrolyte capsules. Small 1:339-348.

19. Toca-Herrera, J. L., S. Moreno-Flores, J. Friedmann, D. Pum, and U. B. Sleytr. 2004. Chemical and thermal denaturation of crystalline bacterial S-layer proteins: an atomic force microscopy study. Microsc. Res. Tech., 65:226-234.

20. Pale-Grosdemange, C., E. S. Simon, K. L. Prime, and G. M. Whitesides. 1991. Formation of self-assembled monolayers by chemisorption of derivatives of oligo(ethylene glycol) of structure HS(CH2)11(OCH2CH2)mOH on gold. Journal of the American Chemical Society, 113:12-20.

21. Bouzide, A., and G. Sauve. 2002. Silver(I) Oxide Mediated Highly Selective Monotosylation of Symmetrical Diols. Application to the Synthesis of Polysubstituted Cyclic Ethers. Organic Letters, 4:2329-2332.

22. Lemieux, R. U., and H. Driguez. 1975. Chemical synthesis of 2-acetamido-2-deoxy-4-O-(.alpha.-L-fucopyranosyl)-3-O-(.beta.-D-galactopyranosyl)-D-glucose. Lewis a blood-group antigenic determinant. Journal of the American Chemical Society, 97:4063-4069.

23. Kolb, H. C., M. G. Finn, and K. B. Sharpless. 2001. Click Chemistry: Diverse Chemical Function from a Few Good Reactions. Angew Chem. Int. Ed. Engl., 40:2004-2021.

24. Sleytr, U. B. & Messner, P. (1989). Self-assembly of bacterial cell surface layers (S-layers). In Electron Microscopy of Subcellular Dynamics, pp. 13-31. Edited by H. Plattner. Boca Raton, FL: CRC Press.

25. Horan, N., L. Yan, H. Isobe, G. M. Whitesides, and D. Kahne. 1999. Nonstatistical binding of a protein to clustered carbohydrates. Proc. Natl. Acad. Sci. U. S. A., 96:11782-11786.

26. Dhayal, M., and D. M. Ratner. 2009. XPS and SPR analysis of glycoarray surface density. Langmuir, 25:2181-2187.

27. Duverger, E., N. Frison, A. C. Roche, and M. Monsigny. 2003. Carbohydrate-lectin interactions assessed by surface plasmon resonance. Biochimie, 85:167-179.

28. Bamdad, C. 1998. The use of Variable Density Self-Assembled Monolayers to Probe the Structure of a Target Molecule. Biophysical Journal, 75:1989-1996.

CHAPTER 4 - NANOBIOFABRICATION OF SURFACE-ENHANCED RAMAN SPECTROSCOPY (SERS) SUBSTRATES USING BACTERIAL SURFACE LAYER PROTEINS

To be submitted to: Journal of American Chemical Society

Surface-enhanced Raman scattering (SERS) has demonstrated extreme potential to be used for chemical and biomolecular sensing and characterization due to its high level of precision and sensitivity (1-4). The magnitude of the enhancement depends on the chemical nature of a molecule adsorbed to a SERS active metallic surface – greatest for silver, gold, and copper. The structure of the metallic material plays an essential role for the SERS phenomenon, in which rougher surfaces are required. Larger SERS effects have been observed for highly ordered metallic nanoparticles with nanoscale gaps between adjacent particles, where signal enhancement factors as large as 10^{12} have been obtained (5). The SERS enhancement has been attributed to both electromagnetic and chemical mechanisms. The electromagnetic mechanism is mainly related to the optical properties of the metallic materials and the large local fields, caused by plasmon resonances that occurs just a few nanometers above the metal surface, resulting in increased Raman scattering. The chemical effect involves the scattering caused by the interaction of the molecule and the metal surface (5). The design of optimized SERS substrates for practical applications remains a challenging process due to the limitations imposed by conventional nano- and micro-fabrication strategies, normally based on "top-down" strategies that are slow and expensive at sub-100 nm scales. Alternatively, several groups have explored bottom-up or self-assembly strategies for the fabrication of SERS substrates with partial success (6, 7), however, the rational design of optimized SERS substrates remains a challenge.

The ability to self-assemble molecules into complex and larger structures is a common manufacturing strategy used by natural systems. Within the last years, great attention has been given to the use of biotemplated nanostructured materials with the so-called "bottom-up" nano- and micro-fabrication strategy as an alternative to conventional nanofabrication strategies (For reviews see (8-11)). Even though the idea

of using biomaterials for nanofabrication appears to be of great potential, a better understanding of these systems and the ability to modify and build custom "biotools" with broader applicability is essential for its full adoption and exploitation.

Bacterial cell surface layer (S-layers) proteins are a great candidate to be used for this purpose. These proteins are found as the outermost structural component in most prokaryotic microorganisms, and the purified monomers possess the ability to reassemble *in vitro* to its original configuration at different physicochemical conditions (*e.g*. solid substrates, air-water interfaces, liposomes, and lipid films) (12, 13). These crystalline arrays are composed of identical monomeric protein (or glycoprotein) with molecular weights that can range from 40-200 kDa depending on the microorganism origin. S-layers display a highly repetitive surface structure with center-to-center lattice spacings of 5-30 nm, and two or more distinct classes of pores with identical morphology and size in the range of 2-8 nm. Here we describe the bionanofabrication of a SERS substrate with the aid of a recombinant variant of the S-layer protein from *Lysinibacillus sphaericus* (SbpA). This approach turned out to be relatively simple and convenient, and potential for future improvement and rational design of new SERS substrates.

Lysinibacillus sphaericus S-layer (SbpA) has been studied in great detail at different levels. SbpA possesses three S-layer homology motifs located in the N-terminal region of the protein that is responsible for anchoring the protein subunits to the secondary cell wall polymers (SCWPs) onto the bacterial cell surface (14). Its crystalline lattice shows a square symmetry, with a center-to-center spacing of the morphological units of 13.1 nm, and the monomers have a molecular weight of 129 kDa. Several works have shown that truncated and fused recombinant SbpA retain their ability to self-assemble *in vitro.*

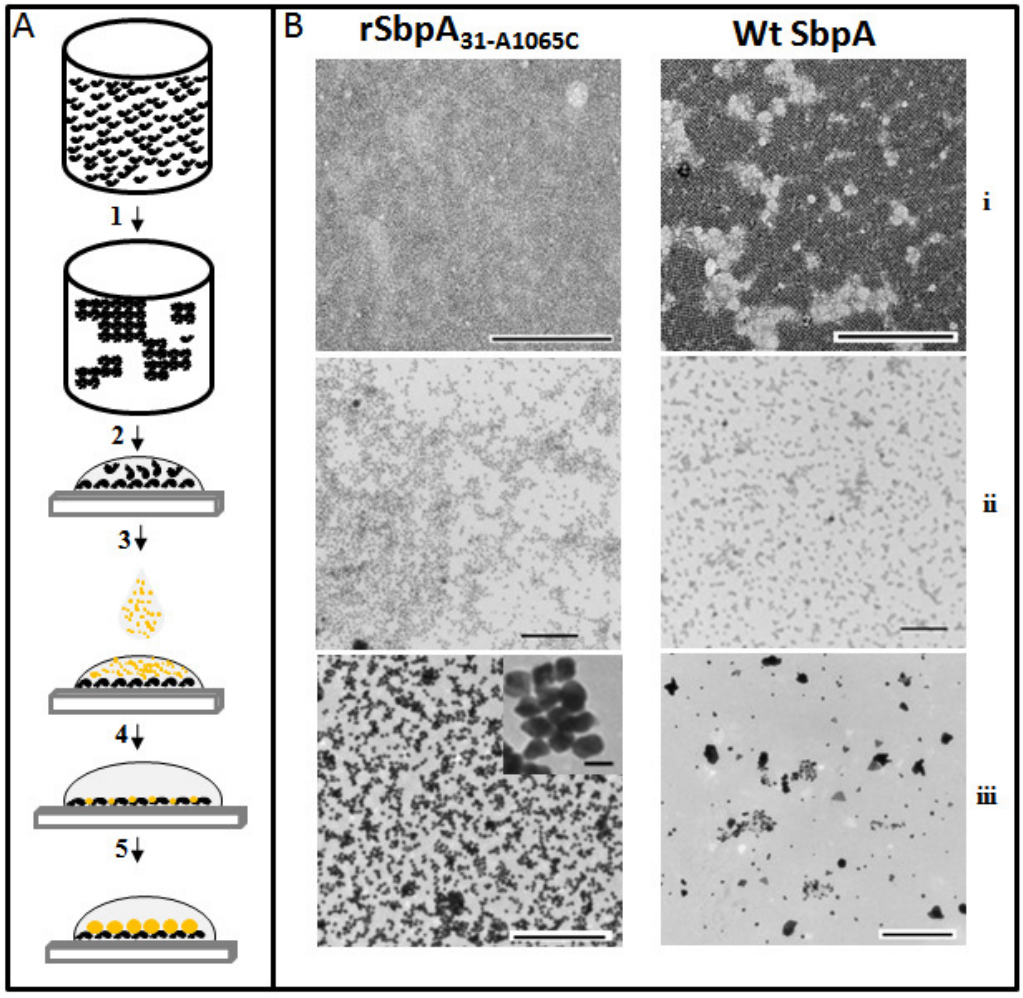

Figure 4.1. (A) Simplified Illustration of the Biotemplating strategy used for the fabrication of SERS substrates, where: 1. SbpA and rSbpA were self-assembled in solution; 2. The assembled products were adsorbed to Silicon chips coated with Poly-lysine; 3. Au NP of 5 nm were adsorbed onto the protein arrays; 4. Non-adsorbed Au NP were rinsed out; 5. Biotemplated Au NP array was enhanced for 5 minutes. (B) TEM images of self-assembled wild type (wt SbpA), and recombinant SbpA ($rSbpA_{31\text{-}A1065C}$). (i) Pure protein adsorbed to the grids and negative-stained. Scale bar = 500 nm. (ii) Biotemplated 5 nm Au NP. Scale bar = 100 nm. (iii) Au NP enhanced for 5 minutes. Scale bar = 500 nm. Inset Scale bar = 25 nm.

In this work we have truncated SbpA by 203 amino acids from the C-terminus of the protein, and a cysteine residue was incorporated as the last residue of the recombinant protein. It was then cloned and overexpressed in *Escherichia coli* and

subsequently purified. rSbpA purity levels higher than 99% were obtained by the protocol established herein, and Ellman's reagent was used to confirm the presence of a single cysteine residue per protein. The SERS substrate bionanofabrication approach used here is briefly illustrated in Figure 1A (for details, see the Supporting information). rSbpA was self-assembled in solution and then adsorbed onto clean Silicon chips pre-coated with poly-Lysine, and subsequently biotemplated with 5 nm pre-synthesized AuNP. After adsorption of the 5 nm AuNP onto the recombinant protein array (mediated by the Au-S interaction between the cysteine residue and AuNP), the samples were extensively rinsed for removal of excess of physisorbed AuNP. The biotemplated AuNPs were then used as catalysts to reduce gold ions onto the individual NPs surface, and consequently enlarging the particles diameter. For direct visualization and analysis of the samples, similar procedures were used on carbon Formvar TEM grids, and the samples observed by TEM. Figure 4.1B shows TEM images of the self-assembled protein (i), the biotemplated Au NP array (ii), and the enhanced biotemplated AuNP (iii). Wild type SbpA was used as control for all the experiments following the same procedures.

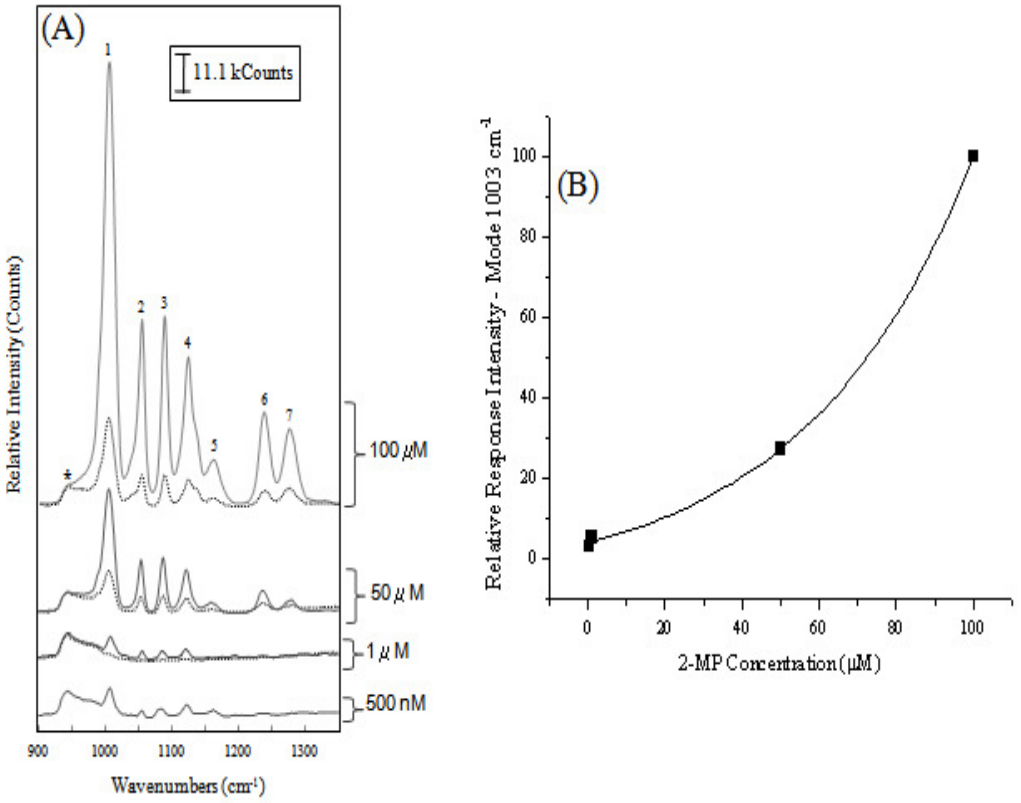

Figure 4.2. (A) Raman spectra of 30 µL of different concentrations (500 nM-100µM) of 2-MP adsorbed on SERS substrates prepared using $rSbpA_{31\text{-}A1065C}$ (Solid lines), and WtSbpA (Dashed lines). * denotes a Silica background Raman mode, and Peaks **1-7** denotes 2-MP Raman modes, where peak **1** is 1003 cm^{-1} mode, peak **2** is 1052 cm^{-1} mode, peak **3** is 1082 cm^{-1} mode, peak **4** is 1122 cm^{-1} mode, peak **5** is 1162 cm^{-1} mode, peak **6** is 1235 cm^{-1} mode, and peak **7** is 1273 cm^{-1}. (**B**) Raman response intensity from the SERS substrate produced using the recombinant SbpA containing 100 µM, 50 µM, 1 µM, and 0.5 µM. All spectra were acquired with a long-range 50× objective, 10 s integration, and 10% laser power (785 nm excitation; 8 mW at 100%). For each parameter tested, 3 spectra were acquired, and their averages shown here.

rSbpA retained the ability to self-assemble and the truncation of 200 amino acids did not interfere with the self-assembly of SbpA as previously shown elsewhere (15). However, we had difficulties obtaining crystals as large as the ones obtained using the same protocol as the one established for the wild type SbpA (Figure 4.1B(i)). Nonetheless, the small crystalline arrays were able to form several small arrays of pre-

synthesized 5 nm AuNP over the entire surface by biotemplating. No apparent AuNP array was observed in the wild-type sample, where just random AuNP aggregates could be seen. Our results are supported by a recent article in which it was shown that the free thiol group of the cysteine residue incorporated at the C-terminus of SbpA was necessary for AuNP biotemplating (15). Interestingly, the small AuNP biotemplated arrays formed onto the rSbpA were not disturbed after the gold enhancement reaction, where AuNP of approximately 20 nm could be obtained (inset in Figure 4.1B(iii) $rSbpA_{31\text{-}A1065C}$). In contrast, large amorphous gold structures were predominantly found in the wild type SbpA samples. Those structures were possibly formed due to the gold enhancement of the random AuNP aggregates present in the samples, which consequently formed single amorphous gold structures per aggregated product.

The performance of the SERS substrates were evaluated by comparing the Raman signal of the adsorbed 2-mercaptopyridine (2-MP) using a Renishaw InVia micro-Raman spectrometer with a long-range 50× objective, with 10 s of integration, and 10 % laser power (785 nm excitation; 8 mW at 100%). An aliquot of 30 µL of different concentrations of 2-MP was added to the SERS substrates and left to dry. Figure 4.2 shows the Raman spectra of 2-MP at concentrations from 0.5 µM to 100 µM. The importance of the AuNP arrays for a high SERS activity was demonstrated, as a difference in the Raman signal between the SERS substrate prepared with the wtSbpA and the $rSbpA_{31\text{-}A1065C}$ was observed. The size of the AuNP in the array is also known to be a critical component for SERS activity (16), where larger AuNP resulted in larger enhancement factors. Interestingly, when arrays of 170 nm AuNP were used as SERS substrate in this article, the appearance of new peaks by SERS was observed. Here, SERS activity was not obtained without enhancing the biotemplated 5 nm AuNP; however after the AuNP were enhanced to approximately 20 nm in

diameter, SERS activity was observed. The SERS activity observed with the wt-SERS was probably caused by the rough surface of the amorphous aggregates formed after the gold enhancement (Figure 4.1b (iii)). At 1 μM of 2-MP, no SERS spectra of 2-MP was observed with the wt-SERS. However, SERS spectra of 30 μL of 500 nM 2-MP could be observed for the substrate prepared with the r-SbpA. At 100 μM the Stokes intensity of the r-SERS was increased to over 120,000 counts for the mode 1003 cm^{-1}, which corresponds to the 2-MP ring breathing. An exponential decrease in the Stokes intensity for the ring breathing mode was observed with decreasing concentrations of 2-MP, reaching the minimum of 3900 counts at 500 nM (Figure 4.2B).

The ability of sensing 500 nM of 2-MP throughout the bionanofabricated SERS substrate was possible even at sub-optimal conditions. To the best of our knowledge, this is the first example of a protein bioinspired SERS active surface using biotemplated AuNP arrays. Nonetheless, the bionanofabrication strategy used here can be significantly improved, as the biotemplated AuNP arrays formed were not large and did not entirely cover the SERS surface with single crystalline arrays (Figure 4.1b (iii)). For the Self-assembly optimization of the r-SbpA, a strategy similar to the one used in Chapter 2 could be used. In addition, the protein self-assembly could be done on a substrate that mimics the bacterial cell surface, which would then allow the formation of larger protein monocrystalline arrays in the correct orientation on a solid substrate: C-terminus exposed to the surface. Our group has shown the potential to mimic the natural SbpA anchor by using self-assembled monolayers (SAMs) containing synthetic carbohydrates (data shown in Chapter 3). Unfortunately, the surfaces with the SAMs that contain carbohydrates mimicking the SbpA natural anchor could not be used in this study, as they are formed on gold substrates, and this surface would interfere with the AuNP enhancing step used here. Another step in which could optimize the homogeneity of the AuNP array is the stringency of rinsing

the non-specific adsorbed AuNP in the biotemplating step. In this step, non-specific adsorption of AuNP on the protein array could be also minimized by using one of the strategies developed by Mark and collaborators (17, 18). Finally, the enhancement of the AuNP could be optimized in a way for reaching the ideal NP size and consequent gap between the NP of the array.

In summary, we have demonstrated the feasibility of bionanofabricating AuNP arrays using recombinant S-layer proteins, which showed SERS activity. Although concentrations of 2-MP as low as 500 nM could be detected by the SERS, we foresee that a lower limit of detection with the same accuracy will be possible with minor optimizations of the bionanofabrication steps employed here.

SUPPORTING INFORMATION

Experimental Methods

Reagents and other chemicals

All aqueous solutions were prepared using reagent grade (18 MΩ cm resistivity) deionized water (DI H_2O) purchased from Stephens Scientific Co. (Riverdale, NJ). Unless stated otherwise, all other reagents and chemicals (ACS grade or better) were purchased either from Aldrich Chemical Co. (Milwaukee, WI) or from Sigma Chemical Co. (St. Louis, MO).

Cloning of Recombinant SbpA (rSbpA-$_{31\text{-}A1065C}$)

DNA manipulations and plasmid constructions were performed according to standard techniques (19). PCR was applied to the genomic DNA from *Lysinibacillus sphaericus* (American type culture collection No. 4525) using High-fidelity DNA polymerase (Invitrogen, Carlsbad, CA) for amplification of rSbpA$_{31\text{-}A1065C}$, and the

oligonucleotides SbpAF31 (**GGGCCC***CCATGG*CGCAAGTAAACGACTATAA CAAAATCTCTGGATA) and SbpAR_A65C (**GGCCGG***GGTACC*TTAGC AAGTAGTTGCTGCCGCATTGTA), which introduced the 5' NcoI, and 3' KpnI restriction sites, respectively. Six random nucleotides were added at the 5' end of both oligonucleotides to allow direct digestion of the PCR product, which was then cloned into the previously linearized plasmid pBAD/*Myc*-HisA (Invitrogen, Carlsbad, CA). The plasmid was previously double digested with KpnI and NcoI, and treated with Shrimp Alkaline Phosphatase (SAP) (Promega, Madison, WI) following the manufacturer's protocol. After ligation for 10 minutes using T4 DNA ligase (New England Biolabs, Ipswich, MA), competent *Escherichia coli* TOP10 cells (Invitrogen, Carlsbad, CA) were transformed with the recombinant plasmid, and incubated overnight. Positive clones were selected and the plasmids purified and sequenced for confirmation of the correct insert.

Expression and Purification of rSbpA$_{31\text{-}A1065C}$ and wild type

rSbpA$_{31\text{-}A1065C}$ was expressed in *E. coli* TOP10 using 1.5 L Erlenmeyer flasks containing 1 L of Luria-Bertani (LB) media supplemented with 50 μg/mL ampicillin. The cells were initially incubated at 37 ^{o}C with constant agitation. Upon reaching an optical density at 600 nm of approximately 0.6, arabinose was added to a final concentration of 0.02% (v/v). After arabinose addition the flask was transferred to another shaker incubator at 30 ^{o}C and kept for an additional 5 hours with constant agitation. The cells were then collected by centrifugation, and rSbpA$_{31\text{-}A1065C}$ purified. Essentially the purification consisted in collecting the insoluble fraction containing rSbpA$_{31\text{-}A1065C}$ that was resuspended with 5 M guanidine hydrochloride, 50 mM Tris-HCl pH 7.2, and the recombinant protein separated from the cell debris by centrifugation 40,000 x *g* for 30 min at 10 ^{o}C. The cleared supernatant containing

$rSbpA_{31\text{-}A1065C}$ monomers was collected and centrifuged again for 2 additional times at 40,000 x *g* for 30 min at 10 ^{o}C. At the end of the centrifugation steps, the clear supernatant was filtered and subjected to size exclusion chromatography using a Superdex 200 Column (GE Healthcare) equilibrated with 3 M guanidine hydrochloride, 50 mM Tris-HCl pH 7.2. Fractions containing the recombinant protein were pooled and dialyzed against DI H_2O. Finally, the solution of purified rSbpA was adjusted to give a protein stock concentration of approximately 0.5 μM and stored at 4 ^{o}C in the presence of 1 mM EDTA. Protein purity was assessed by Coomassie-stained SDS-PAGE.

Self-assembly of $rSbpA_{31\text{-}A1065C}$ and SbpA

All buffer stock solutions were filtered through a nylon membrane (0.22 μm) after preparation and stored at 4 ^{o}C. Samples for the protein self-assembly reactions were prepared by diluting a desired amount of protein stock solution (5 μM SbpA) to a volume of 100 μL with 50 mM Tris pH 9, and 20 mM calcium chloride was added from a 1 M stock solution. The self-assembly reaction was maintained for approximately 5 hrs at RT.

SERS Substrate preparation

Silicon chips were sonicated in acetone, isopropanol, ethanol, and DI water (3 minutes each) for cleaning. Ultra-violet (UV) ozone was used as an additional cleaning step for 1 min. After the cleaning steps, the chips were left in contact with poly-Lysine for 10 min, and subsequently dried with a filter paper. The chips coated with poly-lysine were put in contact with individual droplets of assembled S-layer protein, and left for adsorption for 1 hr. After S-layer adsorption the chips were rinsed with DI water by serial submersions, and then 20 μL of preformed commercial citrate capped 5 nm AuNP (Ted Pella, Inc.) were dropped onto the functionalized substrates

and left for AuNP adsorption for an additional 30 min. Finally the substrates were rinsed, and the adsorbed AuNP were enhanced using the Gold Enhancement kit (Nanoprobes, Inc) for 5 min. following the manufacturer's protocol. After enhancement, the sample was rinsed with DI water and blown dry with N_2, and used as SERS substrates.

Electron Microscopy

The self-assembled protein samples and the biotemplated AuNP were visualized using a Morgagni 268 transmission electron microscope (Philips/FEI Company, Hillsboro, OR) operated at an accelerating voltage of 80 kV. After five hours reassembly in the presence of 50 mM Tris pH 9 and 20 mM calcium chloride droplets of the samples were placed into Petri dish, and 200-mesh carbon-coated Formvar copper TEM grids from Electron Microscopy Sciences (Hatfield, PA), previously coated with 1% poly-Lysine were put in contact with the sample for 1 hr for adsorption. After protein adsorption, the samples were dried with a paper filter. For protein visualization, the samples were negatively stained for 30 seconds with a methylamine tungstate stain from Nanoprobes (Yaphank, NY), and rinsed twice in a droplet of DI H_2O. For biotemplating, the TEM grids with the adsorbed protein were put in contact with droplets of a solution of preformed commercial citrate capped 5 nm AuNP (Ted Pella, Inc.) and left for AuNP adsorption for an additional 30 min. Finally the grids were rinsed, and the adsorbed AuNP were enhanced using the Gold Enhancement kit (Nanoprobes, Yaphank, NY) for 5 min following the manufacturer's protocol. After enhancement, the sample was rinsed with DI water and visualized by TEM.

REFERENCES

1. Bell, S. E., and N. M. Sirimuthu. 2006. Surface-enhanced Raman spectroscopy (SERS) for sub-micromolar detection of DNA/RNA mononucleotides. J. Am. Chem. Soc., 128:15580-15581.

2. Huh, Y. S., A. J. Lowe, A. D. Strickland, C. A. Batt, and D. Erickson. 2009. Surface-enhanced Raman scattering based ligase detection reaction. J. Am. Chem. Soc., 131:2208-2213.

3. Le Ru, E. C., M. Meyer, and P. G. Etchegoin. 2006. Proof of single-molecule sensitivity in surface enhanced Raman scattering (SERS) by means of a two-analyte technique. J. Phys. Chem. B, 110:1944-1948.

4. Strickland, A. D., and C. A. Batt. 2009. Detection of carbendazim by surface-enhanced Raman scattering using cyclodextrin inclusion complexes on gold nanorods. Anal. Chem., 81:2895-2903.

5. Le Ru, E. C., E. Blackie, M. Meyer, and P. G. Etchegoin. 2007. Surface Enhanced Raman Scattering Enhancement Factors: A Comprehensive Study. The Journal of Physical Chemistry C, 111:13794-13803.

6. Tognalli, N., A. Fainstein, E. Calvo, C. Bonazzola, L. Pietrasanta, M. Campoy-Quiles, and P. Etchegoin. 2005. SERS in PAH-Os and gold nanoparticle self-assembled multilayers. J. Chem. Phys., 123:044707.

7. Yan, B., A. Thubagere, W. R. Premasiri, L. D. Ziegler, L. Dal Negro, and B. M. Reinhard. 2009. Engineered SERS Substrates with Multiscale Signal Enhancement: Nanoparticle Cluster Arrays. ACS Nano, 3, 5:1190-1202

8. Park, H., C. Cannizzaro, G. Vunjak-Novakovic, R. Langer, C. A. Vacanti, and O. C. Farokhzad. 2007. Nanofabrication and microfabrication of functional materials for tissue engineering. Tissue Eng., 13:1867-1877.

9. Ai, H., S. A. Jones, and Y. M. Lvov. 2003. Biomedical applications of electrostatic layer-by-layer nano-assembly of polymers, enzymes, and nanoparticles. Cell Biochem Biophys., 39:23-43.

10. Haynie, D. T., L. Zhang, W. Zhao, and J. S. Rudra. 2006. Protein-inspired multilayer nanofilms: science, technology and medicine. Nanomedicine, 2:150-157.

11. Sotiropoulou, S., Y. Sierra-Sastre, S. S. Mark, and C. A. Batt. 2008. Biotemplated Nanostructured Materials. Chemistry of Materials, 20:821-834.

12. Gyorvary, E. S., O. Stein, D. Pum, and U. B. Sleytr. 2003. Self-assembly and recrystallization of bacterial S-layer proteins at silicon supports imaged in real time by atomic force microscopy. J. Microsc., 212:300-306.

13. Wetzer, B., D. Pum, and U. B. Sleytr. 1997. S-layer stabilized solid support lipid bilayers. J. Struct. Biol., 119:123-128.

14. Schaffer, C., and P. Messner. 2005. The structure of secondary cell wall polymers: how Gram-positive bacteria stick their cell walls together. Microbiology, 151:643-651.

15. Jilin, T., B.-L. Helga, E. Andreas, P. Johannes, K. Bernhard, J. G. Hermann, B. S. Uwe, I. Nicola, and H. Peter. 2008. Fabrication of Highly Ordered Gold Nanoparticle Arrays Templated by Crystalline Lattices of Bacterial S-Layer Protein. Chemphyschem, 9:2317-2320.

16. Alexander, W., K. Beomseok, S. Bryce, and L. T. Steven. 2001. Tunable Surface-Enhanced Raman Scattering from Large Gold Nanoparticle Arrays. Chemphyschem, 2:743-745.

17. Mark, S. S., M. Bergkvist, X. Yang, E. R. Angert, and C. A. Batt. 2006. Self-assembly of dendrimer-encapsulated nanoparticle arrays using 2-D microbial S-layer protein biotemplates. Biomacromolecules, 7:1884-1897.

18. Mark, S. S., M. Bergkvist, X. Yang, L. M. Teixeira, P. Bhatnagar, E. R. Angert, and C. A. Batt. 2006. Bionanofabrication of metallic and semiconductor nanoparticle arrays using S-layer protein lattices with different lateral spacings and geometries. Langmuir, 22:3763-3774.

19. Sambrook, J., E. F. Fritsch, and T.Maniatis. 1987. Molecular Cloning: a laboratory manual. Cold Spring Harbor Laboratory Press.

CHAPTER 5 – CONCLUSIONS AND FUTURE DIRECTIONS

In this dissertation we split the work in two main parts, the first dealing fundamental questions which results are reported in Chapter 2 and Chapter 3, and the other area dealing with more applied research, in which the potential use of S-layers for nanobiotechnological applications is reported in Chapter 4. To address the fundamental characteristics that makes SbpA a great candidate to be used in nanobiotechnological applications, on chapter 2 the self-assembly of SbpA was studied with great detail, and on chapter 3 the study of the interaction of SbpA with self-assembled monolayers containing different densities of a synthetic carbohydrate was performed. Finally, on chapter 4, the bionanofabrication of a SERS substrate by the aid of a recombinant SbpA was demonstrated.

By studying the SbpA self-assembly mechanism under different conditions in solution, we found that SbpA undergoes self-assembly at a rate that is dependent on the protein concentration, temperature, and different environmental conditions (i.e., presence/concentration of, calcium, and NaCl). By varying the protein concentration, we could control the formation of polycrystalline versus larger monocrystalline arrays of SbpA in solution. The formation of polycrystalline arrays was generally favored in the presence of high protein concentrations. The data from the kinetics of SbpA self-assembly under the influence of different temperatures implies that this process is entropically driven, and that a net loss of hydrophobic surfaces likely occurs when the SbpA monomeric units are incorporated into the S-layer array. We have also shown that the presence of calcium is necessary for the assembly process; however, at high calcium concentrations the self-assembly rate is dramatically reduced and just small patches of assembled product could be observed by TEM, indicating a deleterious effect of calcium chloride at these levels.

The real time SPR analysis of the interaction of SbpA to mixed SAMs containing the carbohydrate GlcNAc allowed us to study the influence that different

carbohydrate surface densities have on SbpA binding. The critical carbohydrate density was found to be 0.67%, and SAMs containing higher densities of carbohydrates had a negative effect on SbpA binding.

A SERS substrate was produced by biotemplating AuNP with the aid of a recombinant SbpA. Using the bionanofabricated SERS substrate 500 nM of 2-MP by Raman spectroscopy was possible demonstrating the potential of the employed bionanofabrication strategy.

In this dissertation we were able to answer some fundamental questions for the adoption of SbpA in nanotechnological applications. We also demonstrated the flexibility and potential of SbpA for nanofabrication by using a recombinant SbpA for nanofabricating a SERS substrate. However, because of the limitations imposed by the specificity of the SAM to gold surfaces (Chapter 3), and the need for enhancing the AuNP for the SERS substrate (Chapter 4) the full exploitation of the information that we obtained remains restricted. The incompatibility of the system did not allow the use of SAMs containing the critical density of GlcNAc for obtaining larger monocrystalline S-layer arrays and consequently the potential of producing better and more homogeneous SERS substrates.

For future work, because of the flexibility of the synthesized SAM precursors demonstrated here, the interaction of SbpA to other carbohydrates could be studied and then the specificity and characteristic of SbpA-carbohydrate interactions better understood. Additionally, compounds for the formation of SAMs on silicon substrates (e.g. silanes) analogous to the ones used here could be synthesized and substrates mimicking the bacterial surface formed on silicon substrates for the fabrication of the SERS substrates.